Elemental fluorine detection by dielectric barrier discharge coupled to nano-ESI mass spectrometry for non-targeted analysis of fluorinated compounds

Kunyu Zheng, Joseph E. Lesniewski, Michael J. Dolan Jr., Wanqing Li, Tyler T. Metallo, and Kaveh Jorabchi*

Department of Chemistry, Georgetown University, Washington, DC 20057, USA

* Corresponding author: kj256@georgetown.edu, phone: 2026872066

The version of record (edited by the publisher) is available from:

https://doi.org/10.1021/acs.analchem.0c02141

Abstract

The growing use of fluorochemicals has elevated the need for non-targeted detection of unknown fluorinated compounds and transformation products. Elemental mass spectrometry coupled to chromatography offers a facile approach for such analyses by using fluorine as an elemental tag. However, efficient ionization of fluorine has been an ongoing challenge. Here, we demonstrate a novel atmospheric-pressure elemental ionization method where fluorinated compounds separated by GC are converted to Na_2F^+ for non-targeted detection. The compounds are first introduced into a helium dielectric barrier discharge (DBD) for breakdown. The plasma products are subsequently ionized by interaction with a nano-ESI plume of sodium-containing aqueous electrolytes. Our studies point to HF as the main plasma product contributing to Na_2F^+ formation. Moreover, the results reveal that Na_2F^+ is largely formed by the ion-neutral reaction between HF and $Na_2A(NaA)_n^+$, gas-phase reagent ions produced by nano-ESI where A represents the anion of the electrolyte. Near-uniform fluorine response factors are obtained for a wide range of compounds, highlighting good efficiency of HF formation by DBD regardless of chemical structure of the compounds. Detection limits of 3.5 to 19.4 pg fluorine on-column are obtained using the reported GC-DBD-nano-ESI-MS. As an example of non-targeted screening, extractions from oil-and-water-repellent fabrics are analyzed via monitoring Na_2F^+, resulting in detection of a fluorinated compound on a clothing item. Notably, facile switching of the ion source to atmospheric-pressure chemical ionization with the exact same chromatographic method allows identification of the detected compound at the flagged retention time.

Introduction

Fluorinated compounds are mostly anthropogenic and have found growing applications. For instance, it is estimated that 30% of newly approved pharmaceuticals and 30-40% of agrochemicals contain fluorine.[1, 2] Additionally, per- and polyfluoroalkyl substances (PFASs) have been used in a wide variety of industrial and consumer applications, resulting in more than 3000 PFASs on the market.[3] As a consequence of increased usage, fluorinated compounds have been detected in numerous matrices, including water resources and biological samples.[4, 5] Further, various pathways for environmental degradation and metabolism by organisms amplify the diversity of the new and unknown fluorinated compounds.[6] Accordingly, non-targeted analytical techniques are needed to detect these chemicals in a variety of matrices.

Chromatography combined with mass spectrometry (MS) is often used for the detection of these compounds because of their low concentrations. Notably, lack of an isotopic pattern for fluorine raises a challenge in confident detection of unknown compounds in the mass spectra. High-resolution MS is utilized to detect certain classes of compounds such as perfluorinated chemicals via Kendrick mass defect where homologous series are revealed in a sample.[7, 8] Nevertheless, application of this method for non-targeted detection of a broad range of fluorinated compounds, particularly when homologues are not present, remains difficult. Further, the availability of high-resolution MS creates hurdles for many laboratories.

Elemental detection of fluorine in chromatographic separations, on the other hand, offers a universal, non-targeted, and facile approach for screening fluorinated compounds in complex matrices. Commonly, high-sensitivity elemental analysis is performed using inductively coupled plasma (ICP)-MS by creating positive elemental ions within a high-temperature plasma. However, inefficient F^+ formation and isobaric interferences such as $^{18}OH^+$ have hampered fluorine analysis using this technique.[9]

Detection of F^- in ICP-MS has also been investigated as an alternative approach.[10] However, a promising analytical performance using this approach has not been achieved, largely because of isobaric interference from $^{18}OH^-$ and elevated baseline from plasma electrons reaching the detector. These limitations were addressed in our recent reports where chemical ionization of plasma products in the

afterglow of a low-pressure microwave plasma enabled efficient F^- generation from GC-separated organofluorines while minimizing OH^- and electrons as ionization products.[11, 12] Nevertheless, the operation of low-pressure plasma required modification of the MS interface, complicating broad adoption of this technique. Generally, atmospheric-pressure (AP) ionization techniques are preferred because they allow facile coupling to MS instruments and rapid switching between various ionization modes. However, high-sensitivity detection of F^- from AP plasma afterglow is challenging because long transfer times from the AP ionization region to the MS lead to proton transfer reactions of F^- and its neutralization by common acidic plasma products (e.g. HNO_3 and HNO_2).

One approach to address the above-mentioned challenges in elemental fluorine detection is to convert fluorine in the analytes into polyatomic species amenable to spectrometric analysis. Transient species in high-temperature environments have been investigated for this purpose by molecular absorption spectroscopy of GaF in a graphite furnace,[13] molecular emission spectroscopy of SrF in laser induced breakdown,[14] and MS detection of BaF^+ in ICP-MS.[15] In contrast, we have reported a thermodynamically stable and long-lived ion (Na_2F^+) formed in the cooled afterglow of an ICP for elemental fluorine detection.[16] Notably, such long-lived ions enable elemental analysis of fluorine using widely available LC-MS instruments, dramatically improving the adoptability of the technique in various applications.

Here, we report a new approach to form stable polyatomic ions for elemental fluorine detection and apply it to analysis of GC-separated compounds. Importantly, the ionization approach is versatile and provides an avenue to use a wide range of plasmas. In particular, we utilize a dielectric barrier discharge (DBD), a non-thermal plasma with tunability from a reactive plasma for dissociating chemical bonds to soft ionization, offering facile operation and coupling to MS platforms.[17-20] We employ dissociative properties of the DBD to create F-specific plasma products from GC-separated fluorochemicals. The plasma products are then ionized using a nano-ESI, providing a general and non-targeted elemental detection scheme for fluorinated compounds. Our investigations address details of the ion formation mechanism and analytical performance of the technique. Moreover, this approach allows facile toggling between elemental and molecular ionization sources. We demonstrate a proof-of-principle example of this strategy by non-targeted

screening of oil-and-water-repellent fabrics using elemental fluorine detection. Molecular ionization using APCI is then utilized to identify the compounds detected by the elemental screening.

Experimental

Detailed descriptions of the experimental setup and procedures are provided in supporting information (SI) and Figure S1. Below we briefly describe the critical aspects. The schematic of the setup for detecting GC eluates by DBD-nano-ESI-MS is illustrated in Figure 1. The GC column was threaded through and sealed to a steel capillary, which also served as the ground electrode for the DBD. A heated helium gas flow of 100 mL/min was introduced around the capillary and carried the GC eluates into a DBD formed inside a quartz tube (0.6 mm o.d., 0.4 mm i.d.). The plasma was sustained by applying a sinusoidal high voltage to a ring electrode wrapped around the quartz tube at 4 mm downstream of the ground electrode. Unless specified, a peak-to-peak voltage of 2.2 kV at 65 kHz was used to achieve the best analyte breakdown efficiency inside the plasma. The plasma species were characterized via monitoring the optical emission from the DBD by an OSM-400 spectrometer (Newport, Irvine, CA) using an optical fiber. Figure S2 shows the emission spectra, indicating bands attributed to N_2, N_2^+, OH, and O in addition to helium emission lines. These bands indicate the presence of air and water in the helium DBD, possibly from impurities and ambient air diffusion within the gas handling junctions.

The plasma-generated species in the helium flow were diluted by a 2 L/min flow of nitrogen prior to interaction with the nano-ESI plume. The dilution was necessary to minimize discharge-related instabilities in nano-ESI caused by the helium gas. The post-plasma gas dilution was achieved within a ¼" o.d. (4.8 mm i.d.) stainless steel tube inserted into a bored-through tee. The steel tube slid over the quartz plasma tube to direct the nitrogen gas behind the quartz tube outlet. The post-plasma tee and the inserted steel tube were held at +1500 V to direct the ions toward the MS inlet. To ionize plasma products, a pulled borosilicate glass nano-ESI emitter (~5 μm tip i.d.) filled with a 10 mM aqueous electrolyte solution was placed downstream of the post-plasma tee and was biased to about +2300 V (optimized for each experiment). For elemental detection, the ions were monitored in the single-quadrupole mode of a hybrid

MS instrument (QTRAP, based on API2000 platform, Sciex). Molecular identification was achieved by replacing the nano-ESI with a corona discharge needle and utilizing the MS/MS in the triple-quadrupole mode of the instrument. Computational studies were conducted using density functional theory at the ωB97xD/aug-cc-pVTZ level.

All GC samples were prepared in ethyl acetate. 1 μL of sample was injected manually in pulsed splitless mode and separated using a capillary column with a non-polar stationary phase at 2 mL/min He flow rate. For screening applications, approximately 10 mg of fiber from garments was extracted in 1.5 mL ethyl acetate. The sample was analyzed without pre-concentration.

Safety Considerations. High voltages should be used carefully with proper shielding to avoid electrical shocks. Adequate exhaust should be placed above the ionization region to vent plasma products from the lab.

Results and Discussion

Elemental detection of fluorine as Na_2F^+. As noted above, long-lived sodiated ions such as Na_2F^+ provide an attractive avenue for elemental fluorine analysis. In our previous study, aerosolized sodium acetate solutions were introduced into a high-temperature ICP concurrent with fluorinated analytes, resulting in post-plasma formation of NaF.[16] Thermodynamically favorable adduction of NaF with plasma-generated Na^+ yielded Na_2F^+ in the ICP-afterglow. This ionization pathway requires a high plasma gas temperature for efficient desolvation and atomization of sodium acetate aerosol to yield NaF and Na^+, limiting the applicability of many plasma sources and complicating the instrumentation.

To enable generation of stable F-specific ions using various plasma reactors, the experimental setup of Figure 1 was devised. Here, a nano-ESI plume of 10 mM aqueous sodium acetate solution provides sodiation pathways to ionize plasma products of fluorochemicals eluting from GC. Plasma reactions are induced by a non-thermal DBD, operating with a gas temperature close to the ambient room temperature. Markedly, Figure 2 shows that Na_2F^+ is observed from fluorinated compounds of widely different chemical structures using the setup of Figure 1. This observation indicates the conversion of fluorochemicals to a

common precursor by the non-thermal DBD, and subsequent ionization to form Na_2F^+ via interaction with the nano-ESI plume, highlighting a new avenue to use various plasmas for F elemental analysis. Accordingly, the following experiments were conducted to shed light onto the details of the Na_2F^+ ion formation process.

Neutral vs. ionic plasma precursors for Na_2F^+. One mechanism for Na_2F^+ formation is the production of F^- by DBD and subsequent conversion of this ion to Na_2F^+ via interactions with nano-ESI droplets. Although Cl^- has been readily detected from DBD reactions of organochlorines,[20] proton transfer reactions of F^- with acidic plasma products such as HNO_3 make the survival of F^- to the ionization region an unlikely scenario. Nevertheless, we evaluated the potential contribution of F^- to Na_2F^+ formation by implementing post-plasma ion deflection via inserting a wire electrode into the center of the post-plasma steel tube (see Figure S3). This configuration was operated in two modes: 1) iso-potential wire-tube mode (both wire and the tube held at +1500 V) to allow both neutral and charged species to pass through the tube, and 2) biased wire mode (wire +2500 V, tube +1500 V) to collect/deflect ionic species within the post-plasma steel tube, while allowing neutral species to pass through. Calculations based on the electric field, ion mobilities, and gas flow rates provided in SI indicate efficient filtering of the ions in the biased wire mode. Notably, Na_2F^+ intensities detected from various fluorinated compounds were not reduced in the biased wire mode relative to the iso-potential mode (see Figure S4), denoting that ionic species (e.g. F^-) from the DBD do not contribute significantly to Na_2F^+ formation. Thus, we infer that Na_2F^+ is formed by the interaction of neutral plasma reaction products with the nano-ESI plume.

The emergence of Na_2F^+ from fluorinated compounds requires C-F bond breakage in the ion formation process. Considering the high energy of the C-F bond and the low energies available in ionization with ESI and ion sampling, the C-F bond breakage likely occurs within the DBD by high-energy electrons.[21] In other words, we do not anticipate plasma products containing C-F bonds to contribute to the formation of Na_2F^+. Accordingly, we consider F and HF as the DBD reaction products of fluorinated compounds with the potential to lead to Na_2F^+ formation via interaction with the ESI plume.

Importantly, the DBD reaction products carried by gas flows have a significant travel time from the plasma to the ESI tip. The estimates provided in SI indicate a transit time of > 21 ms. On the other hand, a half-life of < 8.7 ms is estimated for atomic F based on the gas-phase reaction of F with the residual water in high purity gases, as discussed in SI. Accordingly, fluorine atoms created by DBD would be converted to HF in transit toward the ESI tip. Therefore, we conclude that HF is the most likely precursor for Na_2F^+ formation in our experiments. We note that HF formation may occur directly within the plasma, via reactions of F with water after the plasma, or via proton transfer to F^- during transit from the plasma plume into the post-plasma tee.

Clustering of Na_2F^+. To optimize Na_2F^+ formation efficiency, we screened the sodium acetate concentration used as the nano-ESI electrolyte. Figure S5 demonstrates that the Na_2F^+ intensity observed from injections of the same amount of a fluorinated compound reaches a plateau at 10 mM sodium acetate. Thus, the ensuing experiments were conducted using 10 mM sodium acetate electrolyte.

Notably, significant clustering of Na^+ with sodium acetate was observed in the background spectra evident from $Na_2CH_3COO(NaCH_3COO)_n^+$ clusters with n = 0-9 in Figure S6a when using 10 mM sodium acetate as nano-ESI electrolyte. Similar clustering of ions has also been observed by others using mM level electrolytes in ESI.[22] A relatively high declustering potential (DP= +75 V) was utilized in our experiments, denoting the stability of these clusters.

Considering the extensive clustering with sodium acetate in the background ions, we examined the possibility of detecting Na_2F^+ clusters with the general formula of $Na_2F(NaCH_3COO)_n^+$ upon injection of fluorinated compounds into the GC. For these experiments, SIM mode detection of clusters with n = 0-9 was utilized with an acquisition rate of 10 Hz to quantitatively capture the transient GC-DBD-nano-ESI-MS signals. Figure 3 illustrates the distribution of $Na_2F(NaCH_3COO)_n^+$ clusters using GC peak areas from injection of decafluorobiphenyl (597 pg F on-column) in relation to distribution of the background cluster ions, confirming the formation of the speculated species. The relevance of clusters from an analytical perspective will be discussed later in the report. In the following, we investigate intensities of clusters with

n = 0-9 to gain insights into the Na_2F^+ formation mechanisms. Clusters with n > 9 had minimal contributions to the total ion intensity of cluster species, thus, they were not included in our analyses.

Na_2F^+ and cluster formation mechanisms. Two main ionization mechanisms could be considered for $Na_2F(NaCH_3COO)_n^+$ formation from HF produced by DBD reactions of fluorinated compounds. The first mechanism is the gas-phase reaction of HF with reagent ions generated by nano-ESI illustrated in Reaction 1, where A represents the anion of the electrolyte used in nano-ESI (e.g. acetate):

$$HF_{(g)} + Na_2A(NaA)_n^+{}_{(g)} \rightarrow Na_2F(NaA)_n^+{}_{(g)} + HA_{(g)} \qquad \textbf{(1)}$$

The second mechanism considers direct interaction of HF with nano-ESI droplets. In this mechanism, HF is captured by charged droplets and is deprotonated via solution-phase reactions. Subsequent solvent evaporation and increase in Na^+ concentration leads to NaF formation, which is then ionized via established ESI pathways (i.e. ion evaporation and charge residue model).

To understand the contributions of these mechanisms, we investigated the effects of various electrolytes in nano-ESI on detection of $Na_2F(NaA)_n^+$. Sodium-containing electrolytes with counter ions of acetate, formate, nitrite, nitrate, and hydroxide were selected, offering varying efficiencies for Reaction 1 and differing solution-phase properties for the droplets-based mechanism. $Na_2F(NaA)_n^+$ formation efficiency was then correlated with the electrolyte characteristics to elucidate which mechanism explains the experimental observations. All electrolytes were prepared at 10 mM to keep sodium concentration constant.

Notably, various electrolytes resulted in differing cluster distributions for $Na_2A(NaA)_n^+$ ions, as shown in Figure S6. Similarly, the electrolytes produced different cluster distributions for $Na_2F(NaA)_n^+$ ions upon injection of fluorinated compounds (Figure S7). Therefore, total $Na_2F(NaA)_n^+$ cluster ion intensity (n=0-9) detected upon injection of the same amount of a fluorinated compound was utilized as a metric to quantify relative $Na_2F(NaA)_n^+$ formation efficiency in various experiments.

Figure 4 depicts the correlation between analyte ion formation efficiency (represented by total detected $Na_2F(NaA)_n^+$) and total reagent ion cluster ($Na_2A(NaA)_n^+$) intensities using various electrolytes.

Below, we consider each mechanism and its consistency with the experimental observations in Figure 4 to decipher the ion formation mechanism.

Gas-phase reaction mechanism. The efficiency of ion formation via reaction 1 is dependent on the energetic favorability of the reaction and the abundance of reagent ions available for ionization. The total reagent ion intensities in the x-axis of Figure 4 reflect the concentrations of reagent ions generated by nano-ESI from each electrolyte. For reagent ions with favorable gas-phase reactions, the ion formation approaches a kinetically controlled regime[23] and a positive correlation is expected between the detected analyte ion and reagent ion intensities. Interestingly, experimental data in Figure 4 follow this expectation except for $NaNO_3$. The deviation of $NaNO_3$ from the trend is explained by reaction energetics, as discussed below.

Reaction 1 is a condensed notation which may include several steps depending on the reagent ion cluster size. In the simpler case of n = 0, the reaction would proceed via collisions of HF with Na_2A^+ forming an initial complex. If the reaction is sufficiently energetic, the reaction products would separate from one another, forming Na_2F^+ and HA. In the case of less favorable reaction energies or larger n, the reaction products may be able to dissipate the reaction energy in vibrational modes and via collisions, leading to the formation of $Na_2F(NaA)_nHA^+$ clusters in the atmospheric ionization region. The clusters would then undergo dissociation upon ion activation in the declustering region of the MS, resulting in Na_2F^+ and $Na_2F(NaA)_n^+$ ions.

Computational investigations provide insights into the energetics of Reaction 1. However, the complexity of the calculations grows rapidly with n, creating uncertainties in the predicted reaction energies. Thus, we have limited our calculations to n = 0, as depicted in Table 1, to decipher relative efficiencies of reagent ions for Na_2F^+ formation via Reaction 1.

The energies in Table 1 indicate that the reaction of HF with all Na_2A^+ ions except for $Na_2NO_3^+$ is favorable. Thus, ion formation efficiency is expected to be low using $NaNO_3$ electrolyte despite significant $Na_2NO_3(NaNO_3)_n^+$ reagent ion intensities. Therefore, the experimental observations in Figure 4 are consistent with the gas-phase reaction mechanism where ionization efficiency is controlled by reagent ion

intensities and reaction energetics. We note that a measurable amount of $Na_2F(NaNO_3)_n^+$ (though very small) is detected despite very unfavorable reaction energy predicted in Table 1. The formation of such unfavorable products may be a result of cluster ion activation in the declustering region of the MS.

HF Ionization by interactions with droplets. This ionization mechanism requires two steps. In the first step, HF is captured by the droplets via deprotonation. In the absence of deprotonation, HF is likely to evaporate from the droplets similar to the solvent. In the second step, the resulting NaF is ionized from the charged droplets. Interestingly, the experimental $Na_2F(NaA)_n^+$ intensities in Figure 4 using various electrolytes also show some correlation with solution properties of electrolyte, indicating potential contribution of the droplets to $Na_2F(NaA)_n^+$ formation. The pKa values in Table 1 show that CH_3COO^-, $HCOO^-$, and NO_2^- can deprotonate HF to varying degrees. For these electrolytes, corresponding clusters of $Na_2F(NaCH_3COO)_n^+$, $Na_2F(NaHCOO)_n^+$, and $Na_2F(NaNO_2)_n^+$ are detected with significant intensities (Figure 4). Moreover, NO_3^- cannot deprotonate HF and does not yield significant $Na_2F(NaNO_3)^+$ intensity (Figure 4). These observations point to the importance of HF deprotonation within the droplets for $Na_2F(NaA)_n^+$ ion formation. NaOH, however, presents a challenge to this notion as one would expect an efficient deprotonation with OH^-, but minimal $Na_2OH(NaOH)_n^+$ is detected using this electrolyte (Figure 4). The discrepancy can be resolved by considering the second step in the droplet-based mechanism. In other words, HF may be efficiently captured and deprotonated in charged NaOH electrolyte droplets, but these droplets may not provide sufficient ionization efficiency for the resulting NaF. To examine the ionization efficiency of NaF from charged droplets, we conducted experiments by spiking 100 μM sodium fluoride into 10 mM electrolyte solutions and directly infused the solutions using nano-ESI.

Figure 5 shows that direct infusion of electrolytes spiked with 100 μM NaF yields far lower $Na_2F(NaA)_n^+$ cluster intensities using 10 mM NaOH as electrolyte compared to when the 10 mM $NaCH_3COO$ electrolyte is utilized. This observation supports the low NaF ionization efficiency from the NaOH electrolyte droplets, providing an explanation for the low analyte ion intensities observed using NaOH. Overall, the relative intensities of $Na_2F(NaA)_n^+$ ions in Figure 4 are also explained by the electrolyte properties in the droplet-based ionization mechanism when both steps are considered.

Relative contributions of the two mechanisms. To delineate the contributions of the two mechanisms, we experimented with electrolytes to find ionization conditions that favor only one of the mechanisms. As noted above, NaOH electrolyte leads to poor ionization in both mechanisms but for different reasons. We hypothesized that the low ionization efficiency of this electrolyte within the mechanism of interaction with droplets may be related to clustering tendencies of NaOH. It is clear from Figure 4 that NaOH electrolyte produces the lowest intensity for its clusters ($Na(NaOH)_n^+$) compared to other electrolytes. To enhance the clustering capabilities while retaining efficient deprotonation, we tested a mixed electrolyte with NaOH and $NaNO_3$ components.

Interestingly, Figure 5 depicts that addition of 10 mM $NaNO_3$ to 10 mM NaOH significantly enhances the ionization of spiked NaF in direct infusion experiments. $Na_2F(NaNO_3)_n^+$ ions are formed in these conditions with an efficiency similar to that of $Na_2F(NaCH_3COO)_n^+$ ions detected from spiked NaF in sodium acetate (see blue bars). Both electrolytes offer efficient HF deprotonation as well. Thus, we infer that $NaCH_3COO$ and $NaOH/NaNO_3$ electrolytes provide similar ionization efficiencies via the droplet-based mechanism. In contrast, $NaOH/NaNO_3$ proves to be an ineffective electrolyte for formation of $Na_2F(NaNO_3)_n^+$ ions via the gas-phase reaction mechanism. This is because $NaOH/NaNO_3$ mainly generates $Na_2NO_3(NaNO_3)_n^+$ reagent ions (see Figure S8), which do not offer favorable energies for ionization of HF via Reaction 1, as discussed before. Upon identification of $NaOH/NaNO_3$ as an electrolyte favoring only ionization by droplets, we tested the effectiveness of this electrolyte in GC-DBD-nano-ESI-MS relative to $NaCH_3COO$, an electrolyte that can provide ionization via both mechanisms.

Figure 5 compares the total $Na_2F(NaA)_n^+$ ion intensities and their identities detected by injections of a fluorinated compound in GC-DBD-nano-ESI-MS using $NaOH/NaNO_3$ and $NaCH_3COO$ electrolytes. Clearly ionization of HF in GC-DBD-nano-ESI greatly favors $NaCH_3COO$ over $NaOH/NaNO_3$ electrolyte (red bars in Figure 5). Notably, $Na_2F(NaCH_3COO)_n^+$ ions detected when using $NaCH_3COO$ electrolyte may form via both mechanisms, while $Na_2F(NaNO_3)_n^+$ ions generated by using $NaOH/NaNO_3$ electrolyte can only be produced via HF interaction with droplets. Further, the two electrolytes provide similar efficiencies in the droplet-based mechanism (blue bars in Figure 5). Therefore, the far higher F detection sensitivity in

GC-DBD-nano-ESI-MS using $NaCH_3COO$ electrolyte indicates greater efficiency of HF ionization via Reaction 1 compared to that obtained via interaction with droplets. It is of note that $NaOH/NaNO_3$ mixture offers improved sensitivities for fluorine detection in GC-DBD-nano-ESI-MS compared to NaOH alone (Figure 5), which itself provides better sensitivities compared to $NaNO_3$ alone (see Figure 4). The improved performance using the mixed electrolyte compared to its components is consistent with the droplet-based ionization mechanism, confirming the contribution of this ionization mechanism.

In summary, both mechanisms contribute to ionization of HF but the gas-phase reactions offer a more efficient pathway, accounting for the vast majority of the $Na_2F(NaA)_n^+$ ions observed in GC-DBD-nano-ESI using electrolytes that produce high intensities of suitable reagent ions (e.g. $NaCH_3COO$ and NaHCOO).

Analytical figures of merit. As illustrated in Figure 4, sodium acetate provides the highest sensitivity for F detection via cluster ion formation in GC-DBD-nano-ESI-MS. Thus, the analytical figures of merit were characterized using this electrolyte. Interestingly, Figure 3 illustrates that the cluster ion with n = 2 has the highest intensity among clusters with n = 0-9, suggesting the stability of this cluster. To determine which cluster offers the best analytical performance, signal-to-noise (S/N) and signal-to-baseline (S/B) ratios were examined by monitoring $Na_2F(NaCH_3COO)_n^+$ for n = 0-9 ions upon injection of a fluorinated compound. GC peak heights were used as signal while baseline and noise were calculated as average and standard deviation of the baseline for 0.1 min prior to the GC peak, respectively. Figure S9 shows the comparison of S/B and S/N between cluster ions. Na_2F^+ (n=0) offers the best analytical performance based on S/B and S/N (Figure S9), despite being the second highest intensity ion in the cluster series (Figure 3). This could be attributed to reduced isobaric interferences at the low m/z of 65. Therefore, the remaining experiments for analytical performance characterization were carried out using Na_2F^+ as the analytical ion for fluorine.

The linear dynamic range for Na_2F^+ formation was tested using 9 fluorinated compounds injected as a mixture at 4 concentration levels, providing a range of 40-1000 pg F on-column. The calibration curves in Figure S10 show linearities with r^2 values of 0.9931-0.9998 for Na_2F^+. Table S2 lists molecular structures

and both elemental and molecular LODs calculated at S/N = 3 using the peak heights for the sample with lowest concentration in linearity studies. A narrow range of elemental LODs (3.5-7.6 pg F on column using most compounds, 19 pg F on column using fludioxonil) are observed despite wide variations in chemical structures, demonstrating analytical utility of this method for a broad range of fluorochemicals, and applicability to analytes beyond those tested in our studies. In contrast, analytical performances of molecular ionization methods differ widely based on molecular properties and ionization conditions, making it difficult to gauge sensitivity of a method a priori for a particular fluorinated compound. For example, tailored-atmosphere DBD afterglow ionization studies have indicated that negative mode ionization within 20% O_2 in He is needed for perfluorohydrocarbons (LODs of 0.8-2.4 pg compound, 0.6-1.9 pg F on-column), while semifluorinated hydrocarbons require positive mode ionization within 20% O_2 in N_2 (LODs of 2-20 pg compound, 0.9-12 pg F on-column).[24] Notably, up to 100-fold deterioration in detection of these compounds is observed when DBD molecular ionization is conducted in open atmosphere.[24] We note that our studies are conducted in open atmosphere using a single experimental condition for detecting compounds with wide-ranging structural features. The good elemental LODs in these experiments highlight the advantages of elemental F detection using Na_2F^+ for non-targeted analysis of fluorochemicals, particularly for compounds with low molecular ionization efficiencies.

We have previously reported better elemental F LODs (~1 pg F on-column) via detection of F^- using low-pressure helium microwave plasma and afterglow chemical ionization in GC-PARCI-MS.[11] However, the atmospheric-pressure operation in the current report offers significant improvements such as ready coupling to many MS platforms and facile switching between elemental and molecular ionization modes. Moreover, we anticipate that analytical performance would be enhanced by controlling the ionization atmosphere (to minimize ambient interferences) and by utilizing more sensitive MS platforms.

Plasma reaction efficiency. For high confidence in non-targeted elemental detection of fluorochemicals, all compounds should ideally yield a common ion (e.g. Na_2F^+) with similar efficiencies regardless of their chemical structures. To investigate this characteristic, we calculated the response factor (RF) for fluorinated compounds of various chemical structures using Equation 2:

$$RF = \frac{GC\ peak\ area\ by\ monitoring\ Na_2F^+}{pg\ F\ on\ Column} \qquad \textbf{(2)}$$

If fluorine is detected with a uniform response factor regardless of chemical structure, we can postulate that the breakdown of molecules to convert fluorine into HF proceeds with close to 100% efficiency. Figure 6 demonstrates the comparison of response factors for compounds in Figure 2 using 2.2 kV and 65 kHz operating parameters for the DBD. Most compounds show similar response factors except for fludioxonil (compound 8 in Figure 6). Interestingly, analogs of this compound sharing a 2,2-difluoro-1,3-benzodioxole motif also show lower than expected RFs (Figure S11). These observations suggest that the breakdown of this structural motif is incomplete within the DBD plasma.

To investigate the impact of DBD operating parameters on uniformity of the RFs, the compounds in Figure 2 were analyzed using DBD operating conditions of 2.2 kV at 22 kHz and 4.1 kV at 22 kHz. Figure S12 shows the response factors in these conditions and compares them to those in Figure 6. The results illustrate that a DBD operated at a higher voltage and frequency yields more uniform response factors, suggesting improved efficiency for analyte conversion to a common plasma product. The effect of frequency may be explained by increased number of micro-discharges per second, enhancing the probability of analyte degradation as they pass through the plasma. Higher voltage could increase the current per discharge as well as the number of micro-discharges per cycle, enhancing the reactivity of the plasma for chemical degradation.[25] Unfortunately, our current DBD driver limited the operations to 65 kHz and 2.2 kV. Improvements in uniformity of response factors may be achieved by utilizing higher power DBD drivers.

Non-targeted analysis of oil-and-water repellent fabrics. Fluorinated polymers are often used as coatings on fabrics to impart oil-and-water repellent properties.[26] These coatings may leach fluorochemicals or detach from the fibers, contributing to environmental contamination. Further, the presence of coatings may be used as a forensic tool to discriminate between fibers with otherwise identical characteristics.[12] To demonstrate the potential of GC-DBD-nano-ESI-MS in non-targeted detection of fluorinated compounds, we applied the technique to screening of leachates from clothing fabrics. Clothing

items were screened by ethyl acetate extraction of 10 mg of fiber from each item followed by analysis using GC-DBD-nano-ESI-MS by monitoring Na_2F^+. An example is shown in Figure 7 for analysis of a Chico's brand shirt where a peak at 5.48 min for Na_2F^+ indicates the presence of a fluorinated compound. A method blank injection is shown in Figure S13, confirming that the peak is specific to the sample.

To identify the detected compound, nano-ESI was replaced with a corona discharge needle operated in positive and negative modes for molecular ionization. In positive mode, a peak at m/z 433 was observed at 5.48 minutes. Figure 7 also shows a chromatogram by monitoring m/z 433, illustrating the elution of this compound at the same retention time as that flagged by the Na_2F^+ detection. Negative mode APCI did not result in any detected ions specific to this retention time, suggesting that the fluorinated compound may not contain an acidic functional group. The MS/MS scan of m/z 433 in positive mode (collision energy = +30 V, 5 spectra/second acquisition rate) shown in Figure 7 suggested a methacrylate ester, yielding protonated mathacrylic acid ($C_4H_7O_2^+$, m/z 87) and its known fragmentation products $[C_4H_7O_2 - H_2O]^+$ (m/z 69) and $[C_4H_7O_2 - CO]^+$ (m/z 59) upon ion activation.[27, 28] Considering that perfluorinated methacrylates are common monomers for fluorinated coatings,[29] we hypothesized that 1H,1H,2H,2H-perfluorooctyl methacrylate (PFOMA, $C_{12}H_9F_{13}O_2$) may be the detected compound because of a close match to the experimental mass of 433 for a protonated ion and experimental isotopic ratios of 12.4% for the [M+1] isotope and 1.2% for the [M+2] isotope. Injecting a standard of PFOMA resulted in the same retention time and fragmentation pattern as those of the sample (see Figure 7 inset), thus confirming the identity of the detected compound from the clothing item.

Conclusions

A new non-targeted approach for the detection of fluorinated compounds is developed to enable screening of fluorochemicals with diverse chemical structures. The technique utilizes a non-thermal plasma with an atmospheric-pressure post-plasma ionization, highlighting facile adoptability and implementation using various plasma sources and MS platforms. Notably, low-resolution MS instruments may be utilized to screen fluorinated compounds in a complex sample using this technique. The screening of fabrics shows

an example of the utility for the technique to selectively flag fluorochemicals in a chromatogram. Importantly, facile switching to molecular ionization allows the identification of the compounds after elemental detection.

The development of this approach is enabled by a fundamental advancement in elemental ionization of F. Namely, plasma reactions are utilized to convert fluorinated compounds into HF with high efficiency. The resulting HF is then ionized via interaction with an ESI plume from a sodium-containing electrolyte to produce Na_2F^+, a stable long-lived ion amenable to detection by many MS platforms. Both charged droplets and gas-phase ions produced by the ESI contribute to the formation of Na_2F^+. Importantly, the counter ion for the sodium-containing electrolyte plays a key role in analyte ion formation efficiency. Tendencies of the electrolytes to form clusters with Na_2F^+ in the charged droplets enhance ionization of NaF produced upon deprotonation of HF in the droplet. In the gas-phase reaction mechanism, the density of $Na_2A(NaA)_n^+$ cluster ions and their energetic favorability to react with HF determine the sensitivity of the method. Our investigations suggest that the reaction of HF with gas-phase ions is a more efficient ionization pathway. Among the tested electrolytes, sodium acetate offers the best sensitivity for fluorine detection because of facile generation of reactive clusters. These fundamental insights also provide avenues to further enhance the performance of the technique. For example, other plasma types and plasma geometries may be utilized to enhance the efficient transfer of HF to the ionization region. Steps to improve reagent ion density is also expected to enhance the ionization of HF.

Acknowledgments

This material is based upon work supported by National Science Foundation (NSF) under grant CHE-1904835. Michael J. Dolan Jr. was supported by Award No. 2017-R2-CX-0007, awarded by the National Institute of Justice, Office of Justice Programs, U.S. Department of Justice. We thank PerkinElmer Inc. for the loan of the GC.

Conflict of interest

Kaveh Jorabchi, Joseph Lesniewski, and Kunyu Zheng are inventors on a U.S. provisional patent application and Kaveh Jorabchi is an inventor on US patent 9,966,243 related to the technique described in this report.

Supporting Information

Experimental procedures, optical emission of DBD, calculations related to ion deflection efficiency and post-plasma reactions of fluorine atom, effect of sodium acetate concentration on Na_2F^+ formation, mass spectra and cluster distributions for various electrolytes, total reagent ion intensity for mixed $NaOH/NaNO_3$ electrolyte, S/N and S/B using $Na_2F(NaCH_3COO)_n^+$ as analyte ions, calibration curves by monitoring Na_2F^+, Table of LODs, response factor of fludioxonil analogs, effect of DBD operating parameters on Na_2F^+ response factor, chromatogram for method blank, and Gaussian output files for optimized geometries.

References

1. Zhou, Y.; Wang, J.; Gu, Z.; Wang, S.; Zhu, W.; Acena, J. L.; Soloshonok, V. A.; Izawa, K.; Liu, H., Next Generation of Fluorine-Containing Pharmaceuticals, Compounds Currently in Phase II-III Clinical Trials of Major Pharmaceutical Companies: New Structural Trends and Therapeutic Areas. *Chem. Rev.* **2016,** *116* (2), 422-518.

2. Fujiwara, T.; O'Hagan, D., Successful fluorine-containing herbicide agrochemicals. *J. Fluor. Chem.* **2014,** *167*, 16-29.

3. Wang, Z.; DeWitt, J. C.; Higgins, C. P.; Cousins, I. T., A Never-Ending Story of Per- and Polyfluoroalkyl Substances (PFASs)? *Environ. Sci. Technol.* **2017,** *51* (5), 2508-2518.

4. Richardson, S. D.; Kimura, S. Y., Water Analysis: Emerging Contaminants and Current Issues. *Anal. Chem.* **2020,** *92* (1), 473-505.

5. Poothong, S.; Thomsen, C.; Padilla-Sanchez, J. A.; Papadopoulou, E.; Haug, L. S., Distribution of Novel and Well-Known Poly- and Perfluoroalkyl Substances (PFASs) in Human Serum, Plasma, and Whole Blood. *Environ. Sci. Technol.* **2017,** *51* (22), 13388-13396.

6. Joudan, S.; Liu, R.; D'Eon, J. C.; Mabury, S. A., Unique analytical considerations for laboratory studies identifying metabolic products of per- and polyfluoroalkyl substances (PFASs). *TrAC Trends Anal. Chem.* **2020,** *124*, 115431.

7. Barzen-Hanson, K. A.; Roberts, S. C.; Choyke, S.; Oetjen, K.; McAlees, A.; Riddell, N.; McCrindle, R.; Ferguson, P. L.; Higgins, C. P.; Field, J. A., Discovery of 40 Classes of Per- and Polyfluoroalkyl Substances in Historical Aqueous Film-Forming Foams (AFFFs) and AFFF-Impacted Groundwater. *Environ. Sci. Technol.* **2017,** *51* (4), 2047-2057.

8. Bugsel, B.; Zwiener, C., LC-MS screening of poly- and perfluoroalkyl substances in contaminated soil by Kendrick mass analysis. *Anal Bioanal Chem* **2020**, DOI:10.1007/s00216-019-02358-0

9. Flores, E. M. M.; Mello, P. A.; Krzyzaniak, S. R.; Cauduro, V. H.; Picoloto, R. S., Challenges and Trends for Halogen Determination by Inductively Coupled Plasma Mass Spectrometry: A Review. *Rapid Commun. Mass Spectrom.* **2020,** e8727, DOI: 10.1002/rcm.8727.

10. Vickers, G. H.; Wilson, D. A.; Hieftje, G. M., Detection of negative ions by inductively coupled plasma mass spectrometry. *Anal. Chem.* **1988,** *60* (17), 1808-1812.

11. Wang, H.; Minardi, C. S.; Badiei, H.; Kahen, K.; Jorabchi, K., High-sensitivity elemental ionization for quantitative detection of halogenated compounds. *Analyst* **2015,** *140* (24), 8177-85.

12. Dolan, M. J., Jr.; Blackledge, R. D.; Jorabchi, K., Classifying single fibers based on fluorinated surface treatments. *Anal Bioanal Chem* **2019,** *411* (19), 4775-4784.

13. Qin, Z.; McNee, D.; Gleisner, H.; Raab, A.; Kyeremeh, K.; Jaspars, M.; Krupp, E.; Deng, H.; Feldmann, J., Fluorine speciation analysis using reverse phase liquid chromatography coupled off-line to continuum source molecular absorption spectrometry (CS-MAS): identification and quantification of novel fluorinated organic compounds in environmental and biological samples. *Anal. Chem.* **2012,** *84* (14), 6213-9.

14. Tang, Z.; Zhou, R.; Hao, Z.; Zhang, W.; Li, Q.; Zeng, Q.; Li, X.; Zeng, X.; Lu, Y., Determination of fluorine in copper ore using laser-induced breakdown spectroscopy assisted by the SrF molecular emission band. *J. Anal. At. Spectrom.* **2020,** *35*, 754-761.

15. Jamari, N. L. A.; Dohmann, J. F.; Raab, A.; Krupp, E. M.; Feldmann, J., Novel non-targeted analysis of perfluorinated compounds using fluorine-specific detection regardless of their ionisability (HPLC-ICPMS/MS-ESI-MS). *Anal. Chim. Acta* **2019,** *1053*, 22-31.

16. Lesniewski, J. E.; Zheng, K.; Lecchi, P.; Dain, D.; Jorabchi, K., High-Sensitivity Elemental Mass Spectrometry of Fluorine by Ionization in Plasma Afterglow. *Anal. Chem.* **2019,** *91* (6), 3773-3777.

17. Klute, F. D.; Schütz, A.; Brandt, S.; Burhenn, S.; Vogel, P.; Franzke, J., Characterization of dielectric barrier discharges for analytical chemistry. *J. Phys. D: Appl. Phys.* **2018,** *51* (31).

18. Gyr, L.; Wolf, J. C.; Franzke, J.; Zenobi, R., Mechanistic Understanding Leads to Increased Ionization Efficiency and Selectivity in Dielectric Barrier Discharge Ionization Mass Spectrometry: A Case Study with Perfluorinated Compounds. *Anal. Chem.* **2018,** *90* (4), 2725-2731.

19. Kunze, K.; Miclea, M.; Franzke, J.; Niemax, K., The dielectric barrier discharge as a detector for gas chromatography. *Spectrochim. Acta Part B* **2003,** *58* (8), 1435-1443.

20. Zheng, K.; Dolan, M. J., Jr.; Haferl, P. J.; Badiei, H.; Jorabchi, K., Atmospheric-Pressure Dielectric Barrier Discharge as an Elemental Ion Source for Gas Chromatographic Analysis of Organochlorines. *Anal. Chem.* **2018,** *90* (3), 2148-2154.

21. Kim, Y.; Hong, S. H.; Cha, M. S.; Song, Y.-H.; Kim, S. J., Measurements of electron energy by emission spectroscopy in pulsed corona and dielectric barrier discharges. *J. Adv. Oxid. Technol.* **2003,** *6* (1), 17-22.

22. Hao, C.; March, R. E.; Croley, T. R.; Smith, J. C.; Rafferty, S. P., Electrospray ionization tandem mass spectrometric study of salt cluster ions. Part 1—investigations of alkali metal chloride and sodium salt cluster ions. *J. Mass Spectrom.* **2001,** *36* (1), 79-96.

23. Sunner, J.; Nicol, G.; Kebarle, P., Factors determining relative sensitivity of analytes in positive mode atmospheric pressure ionization mass spectrometry. *Anal. Chem.* **1988,** *60* (13), 1300-1307.

24. Vogel, P.; Marggraf, U.; Brandt, S.; Garcia-Reyes, J. F.; Franzke, J., Analyte-Tailored Controlled Atmosphere Improves Dielectric Barrier Discharge Ionization Mass Spectrometry Performance. *Anal. Chem.* **2019,** *91* (5), 3733-3739.

25. Müller, S.; Krähling, T.; Veza, D.; Horvatic, V.; Vadla, C.; Franzke, J., Operation modes of the helium dielectric barrier discharge for soft ionization. *Spectrochim. Acta Part B* **2013,** *85*, 104-111.

26. Zahid, M.; Mazzon, G.; Athanassiou, A.; Bayer, I. S., Environmentally benign non-wettable textile treatments: A review of recent state-of-the-art. *Adv Colloid Interface Sci* **2019,** *270*, 216-250.

27. Gjøs, N.; Urdal, K.; Ruyter, I. E.; Sjøvik, I. J., Identification of methacrylates and acrylates in dental materials by mass spectrometry. *Analytica Chimica Acta* **1983,** *149*, 87-99.

28. Harrison, A. X.; Ichikawa, H., Site of protonation in the chemical ionization mass spectra of olefinic methyl esters. *Organic Mass Spectrometry* **1980,** *15* (5), 244-248.

29. Yao, W.; Li, Y.; Huang, X., Fluorinated poly(meth)acrylate: Synthesis and properties. *Polymer* **2014,** *55* (24), 6197-6211.

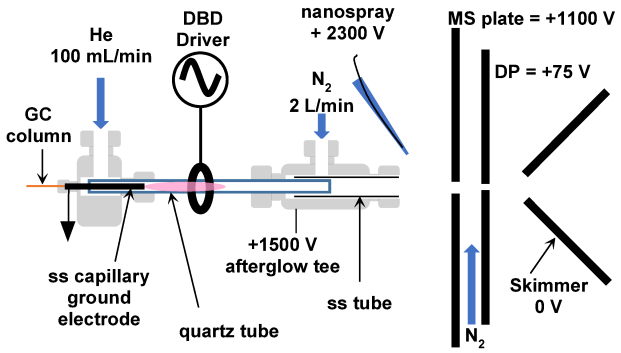

Figure 1. Schematic of DBD-nano-ESI-MS for elemental detection of GC eluates.

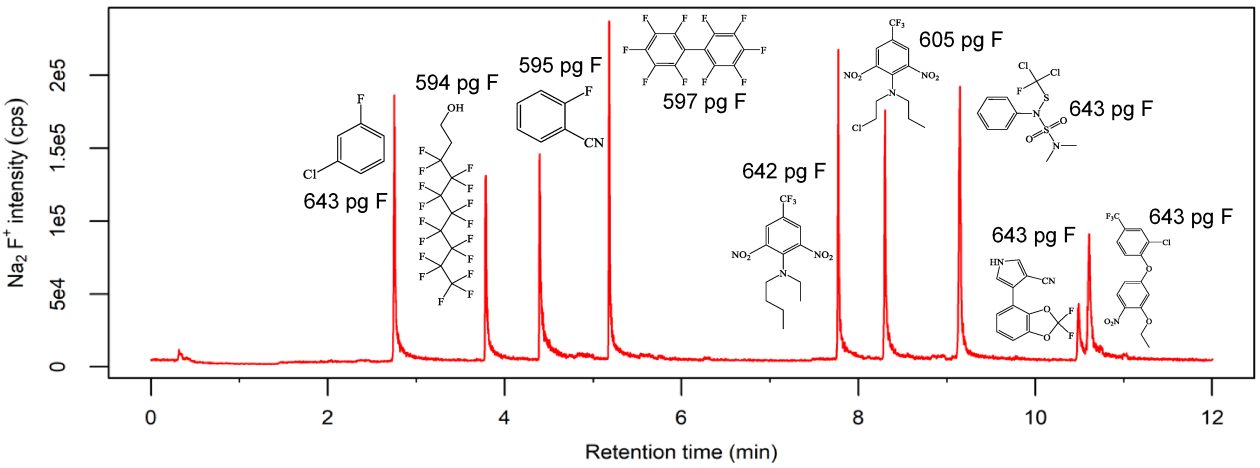

Figure 2. Fluorinated compounds detected as Na_2F^+ in GC-DBD-nano-ESI-MS using 10 mM sodium acetate as nano-ESI solution. Structures and injection amounts on-column are labeled next to each peak (see Table S1 for compound names).

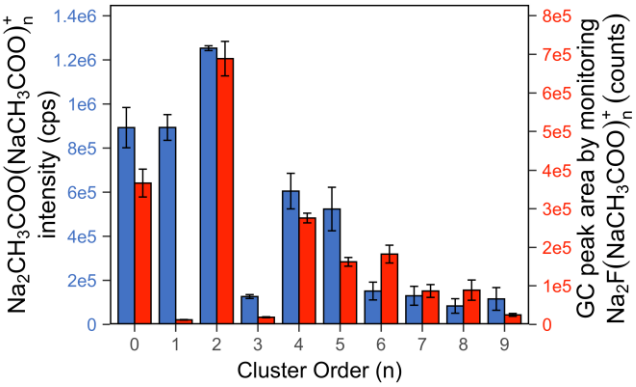

Figure 3. Cluster distributions of electrolyte and analyte ions. $Na_2CH_3COO(NaCH_3COO)_n^+$ electrolyte cluster intensities generated from 10 mM sodium acetate in nano-ESI are shown in blue bars (left axis). $Na_2F(NaCH_3COO)_n^+$ analyte cluster distribution is represented in red bars (right axis) based on GC peak areas detected from injections of decafluorobiphenyl (597 pg F on-column) in GC-DBD-nano-ESI-MS using 10 mM sodium acetate in nano-ESI. Error bars indicate standard deviations of ion intensities and GC peak areas from three experiments with a different nano-ESI tip used in each experiment.

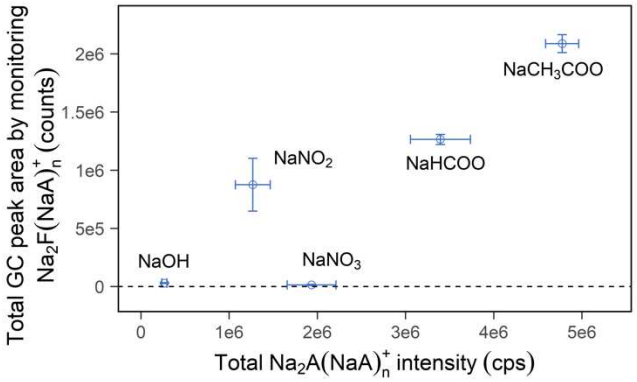

Figure 4. Total GC peak area by monitoring $Na_2F(NaA)_n^+$ cluster intensities with n = 0-9 as a function of the total reagent ion cluster intensities ($Na_2A(NaA)_n^+$ with n = 0-9) using various electrolytes. $Na_2F(NaA)_n^+$ clusters were detected via injections of decafluorobiphenyl (597 pg F on-column) in GC-DBD-ESI-MS. Error bars indicate standard deviations of ion intensities and GC peak areas from three experiments with a different nano-ESI tip used in each experiment.

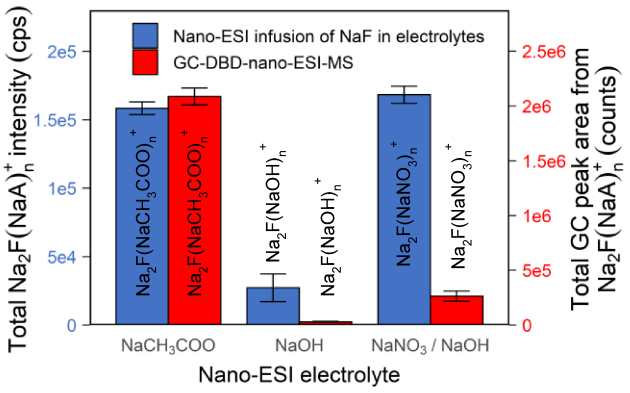

Figure 5. Effect of electrolyte on $Na_2F(NaA)_n^+$ formation in direct nano-ESI infusion (blue bars, left y axis) and GC-DBD-nano-ESI-MS. Clusters with n = 0-9 were used. Direct infusion was conducted using 100 µM NaF spiked in 10 mM electrolytes. GC-DBD-nano-ESI-MS peak areas were based on total cluster ion intensities detected from injections of decafluorobiphenyl (597 pg F on-column) (red bars, right y axis). Error bars indicate standard deviations of ion intensities and GC peak areas from three experiments with a different nano-ESI tip used in each experiment.

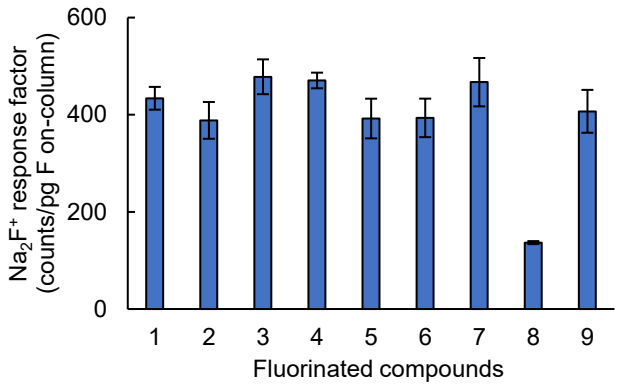

Figure 6. Na_2F^+ response factors for fluorinated compounds using DBD operated at 2.2 kV and 65 kHz. X-axis indicates compounds in the order of elution in Figure 2 (see Table S1 for compound names). The on-column injection amounts are the same as those in Figure 2. Error bars represent standard deviations based on triplicate injections.

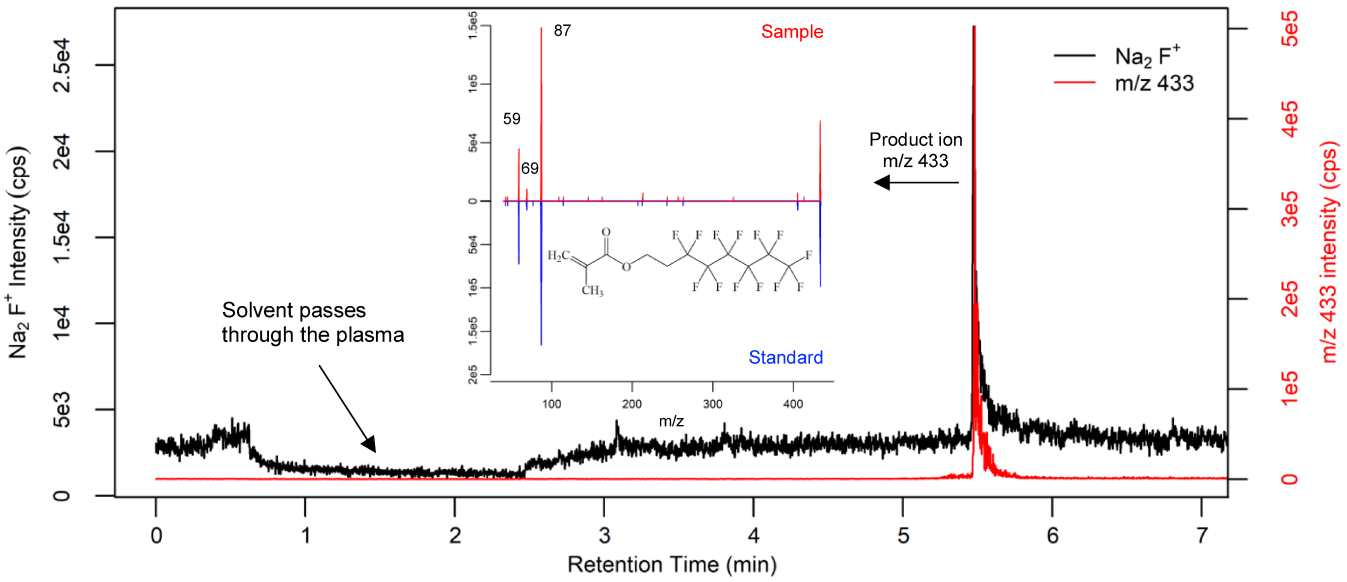

Figure 7. Overlaid chromatograms for a fiber sample from a Chico's brand shirt by monitoring Na_2F^+ (black trace) in GC-DBD-nano-ESI-MS and m/z 433 in GC-APCI-MS (red trace). The inset compares product-ion spectra of m/z 433 in the sample to that of PFOMA standard both obtained at retention time of 5.48 minutes.

Table 1. Calculated energies for Reaction 1 (n=0) and solution-phase acidities of the protonated electrolyte anions.

Electrolyte anion (A^-)	ΔH_{298K} (kJ/mol)	ΔG_{298K} (kJ/mol)	pK_a of HA*
CH_3COO^-	-17.4	-11.7	4.76
$HCOO^-$	-9.39	-4.49	3.74
NO_2^-	-2.50	-3.54	3.15
NO_3^-	41.7	39.5	< 0
OH^-	-89.1	-86.6	14
F^-	-	-	3.17

* taken from Smith, R.; Martell, A.; Motekaitis, R., NIST Standard Reference Database 46. **2001**.

Graphical abstract

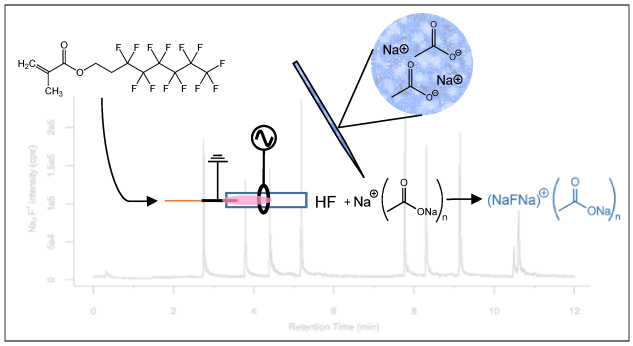

Supporting Information

Elemental Fluorine Detection by Dielectric Barrier Discharge Coupled to Nano-ESI Mass Spectrometry for Nontargeted Analysis of Fluorinated Compounds

Kunyu Zheng, Joseph E Lesniewski, Michael J. Dolan Jr., Wanqing Li, Tyler T. Metallo, and Kaveh Jorabchi*

Department of Chemistry, Georgetown University, Washington, DC 20057, USA

* Corresponding author: kj256@georgetown.edu, phone: 2026872066

Table of Contents

Experimental details

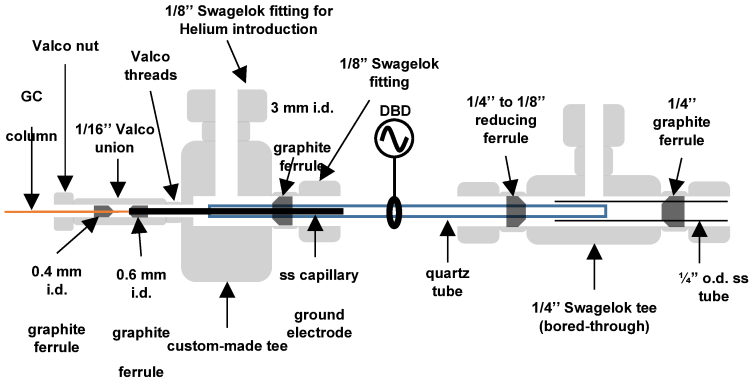

Figure S1. Details of the interface for guiding GC eluates into a helium DBD and subsequent post-plasma dilution with nitrogen gas.

A stainless-steel capillary (0.6 mm o.d., 0.4 mm i.d., 3.5 cm long) surrounded the GC column and acted as the ground electrode for DBD. The GC column was first passed through a 1/16" union (Valco ZT2L, VICI, Houston, TX) and was sealed on the left side using a graphite ferrule as shown in Figure S1. The other side of the union was threaded to one port of a custom-made steel tee serving as the nut for the union. A graphite ferrule sealed the steel capillary at this junction and held it concentric to the gas channel of the tee. A quartz tube (3 mm o.d., 1 mm i.d., 5 cm long) was sealed to the opposite port of the tee using a graphite ferrule (1/4'' to 1/16'' reducing ferrule) while helium plasma gas (99.995%) was delivered at 100 mL/min by a mass flow controller (Model 246B, MKS, Andover, MA) to the orthogonal port of the tee. The tee was grounded and was heated to 250 °C.

The length of the steel capillary and the GC column were adjusted so that the column was flush with the steel capillary outlet and the end of the capillary was positioned 2 cm inside the quartz tube. A ring electrode surrounding the quartz tube was placed 4 mm downstream of the steel capillary end. This distance was selected to maximize the length of the plasma for increased analyte residence time while minimizing the likelihood of discharge from the ring electrode to the post-plasma tee. A thorough optimization of this

distance was not conducted although movements of ~1 mm in either direction did not produce significant changes in analytical signal in our screening experiments. A high voltage sinusoidal waveform was applied to the ring electrode by a DBD power supply (PVM500, Information Unlimited, Amherst, NH), resulting in formation of a pin-to-ring DBD. The power supply was operated at peak-to-peak voltage of 2.2 kV and 65 kHz for best plasma reaction efficiency. The voltage and frequency of the power supply were measured using a high-voltage probe (Tektronix P6015A) with 1000x setting connected to a digital oscilloscope.

To minimize effects of helium plasma gas on nano-ESI operation, the 100 mL/min helium flow carrying the DBD-generated species out of the quartz tube was mixed with 2 L/min of nitrogen gas (supplied by a mass flow controller Model 246B, MKS, Andover, MA) within a 1/4" bored-through tee (SS-400-3BT; Swagelok, Solon, OH) as shown in Figure S1. A ¼" stainless-steel tube (4.8 mm i.d.) was sealed to the tee using a graphite ferrule (1/4'' graphite ferrule) and extended over the plasma quartz tube to ensure that the N_2 flow was directed behind the quartz tube, minimizing turbulence and loss of neutrals to the steel tube walls. The whole post-plasma tee assembly was held at +1500 V to create a proper electric field for ion transport toward the MS.

A pulled borosilicate glass nano-ESI tip (i.d.: ~5 μm, prepared using a capillary puller, PN-3, Narishige Scientific Instrument Lab, Tokyo, Japan) was positioned about 1 mm above the post-plasma steel tube at 45° angle, 5 mm downstream of the nitrogen tee and 15 mm from the MS plate. 10 mM aqueous solutions of various electrolytes were sprayed in our experiments by applying around 2300 V to the solution inside the nano-ESI emitter using a stainless-steel wire inserted into the back of the emitter. The exact voltage was optimized for each experiment to establish a stable spray.

Gas chromatograph. An Agilent 6890 GC (Santa Clara, CA) equipped with a split/splitless injector (275 °C, column flow = 2 mL/min He) and a capillary column (5%-phenyl-95%-dimethyl polysiloxane, 30 m×0.250 mm, 0.25 μm film thickness, Elite-5 MS II, PerkinElmer, Waltham, MA) was used in the investigations. 1-μL injections were conducted in pulsed splitless mode with a pulse pressure of 40 psi for 0.4 min. The oven temperature was held at 55 °C for 2.5 minutes, then ramped to 215 °C at 15 °C/min, then to 240 °C at 6 °C/min, and to 280 °C at 30°C/min, where it was held for 1 minute. For non-

targeted analysis of fibers, the oven temperature program followed the same rates and set points with the exception that a starting temperature of 40 °C was utilized.

Mass spectrometer. Ions were detected using a hybrid MS (QTRAP based on API2000 platform, Sciex, Framingham, MA). A constant curtain plate voltage of +1100 V was supplied by the instrument at counterflow gas setting of 10 (arbitrary units). The ion sampling plate of the MS was held at +75 V (DP = 75), the skimmer was grounded, and the ion transmission RF quadrupole was biased to -10 V for optimal declustering of ions and transmission to the mass analyzer. Background ion scans were conducted using a Q1 scan from m/z 10 to 1000 in 3 s (10 points per mass) to identify the clusters generated by nano-ESI. For F elemental analysis, Q1 selected ion monitoring (SIM) was utilized and the dwell times were adjusted to record ion intensities at 10 Hz. For molecular identification, nano-ESI was replaced by a corona discharge (+4300 V, 2 μA for positive and −3800 V, 12 μA for negative mode) and the DBD was turned off to provide atmospheric pressure chemical ionization (APCI) of GC eluates. A 5 Hz acquisition rate was used for Q1 scans from m/z 100 to 800 with a DP voltage of 15 V to detect ions.

Electrolytes and sample preparation. Sodium hydroxide (IC eluent grade), sodium acetate trihydrate (ACS reagent grade), and sodium formate (analytical standard) used for nano-ESI electrolytes were from Sigma-Aldrich (St. Louis, MO, USA). Sodium nitrate (ACS reagent grade) and sodium nitrite (ACS reagent grade) were purchased from Fisher Scientific (Waltham, MA). All electrolyte solutions were prepared at 10 mM in 18 MΩ water from stock solutions of ~50 mg/mL (made in house), except for NaOH whose 0.1 M stock solution was purchased directly from the supplier noted above. The electrolyte solutions were stored in room temperature. The analytical standards included 1H,1H,2H,2H-perfluoro-1-decanol, 2-fluorobenzonitrile and decafluorobiphenyl (Oakwood Chemicals, West Columbia, SC, USA), benfluralin, dichlofluanid, oxyfluorfen and fludioxonil (AccuStandard, New Haven, CT, USA), 1-chloro-3-fluorobenzene and fluchloralin, (Sigma-Aldrich), and 1H,1H,2H,2H-perfluorooctyl methacrylate (Fluoryx Labs, Carson City, NV). Stock solutions of all analytes except for fludioxonil were prepared by dissolving 10-50 mg compound in 1 mL ethyl acetate (Sigma-Aldrich). Stock solution of fludioxonil was purchased

as 100 μg/mL solution in methanol from the supplier listed above. Analytical standards were prepared by dilutions of stock solutions in ethyl acetate. All analytical solutions were stored at 4 °C.

For non-targeted detection of extracted fluorinated compounds from fabrics, approximately 10 mg of fiber from clothing items was weighed into a 2-mL glass vial and soaked in 1.5 mL ethyl acetate for 1h with occasional vortex. The extract was filtered using a 0.45 μm nylon filter (AutoPack Tube, PALL, New York, NY) and directly injected into the GC.

Density functional theory calculations. The molecular geometries were optimized at the theory level of ωB97xD/aug-cc-pVTZ using Gaussian16 package.[1] Enthalpies and Gibbs free energies of reactions were calculated at 298 K using the values adjusted for thermal and zero point energies by the package. The output files for all considered species are supplied as supporting information in .txt format. The file extensions may be changed to .out for viewing using molecular modeling packages.

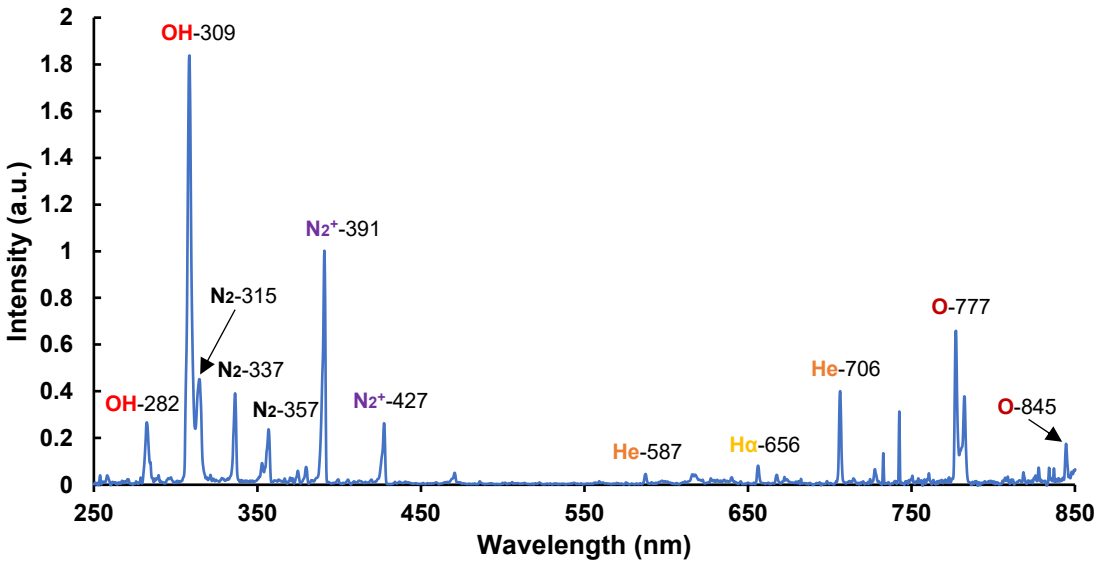

Figure S2. Optical emission spectrum of pin-to-ring He-DBD operated at 2.2 kV and 65 kHz with wavelengths and species assigned based on well-characterized emission lines.[2] The spectrum is acquired using a OSM-400 spectrometer (Newport, Irvine, CA) equipped with an optical fiber (400-μm core size, 0.22 numerical aperture; Newport, Irvine, CA) whose end was placed 5 mm away from the quartz tube in a side-viewing geometry. The nitrogen bands may originate from nitrogen impurity in helium or air diffusion into plasma gas within gas handling junctions. OH emission indicates the presence of water in the plasma.

Table S1. Names of compounds and elution times in Figure 2

Elution order	Retention time (min)	Compound (CAS #)
1	2.75	1-chloro-3-fluorobenzene (625-98-9)
2	3.79	1H,1H,2H,2H-perfluoro-1-decanol (678-39-7)
3	4.40	2-fluoro-benzonitrile (394-47-8)
4	5.18	Decafluorobiphenyl (434-90-2)
5	7.77	Benfluralin (1861-40-1)
6	8.30	Fluchloralin (33245-39-5)
7	9.15	Dichlofluanid (1085-98-9)
8	10.49	Fludioxonil (131341-86-1)
9	10.61	Oxyfluorfen (42874-03-3)

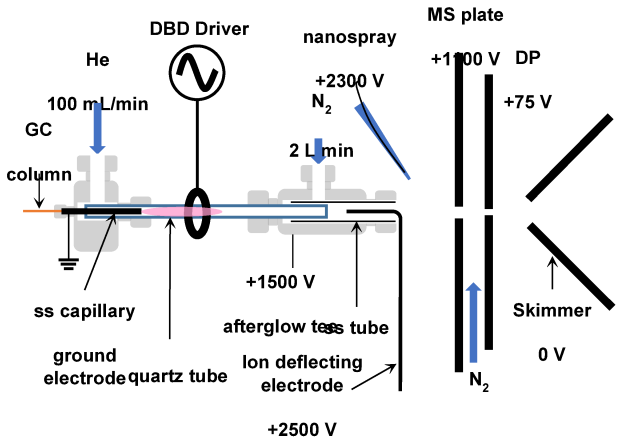

Figure S3. Schematic of DBD-nano-ESI with ion deflection electrode. A 2-cm long wire (o.d. 0.76 mm) is inserted into the center of the post-plasma steel tube carrying the nitrogen-helium flow. To deflect the ions within the tube, the wire is biased to +2500 V while the tube is held at +1500 V. For passing ions, both wire and the tube are held at +1500 V.

Ion deflection efficiency

To evaluate the efficiency of ion deflection, we first calculate the time required for the ions to travel between the wire electrode and the inner surface of the post-plasma steel tube in the biased wire mode as a result of the electric field between the two electrodes. We then compare this value to the time it takes for the ions to be carried by the gas flows through the deflector. If the time needed for ion travel induced by the electric filed is significantly lower than the time for the gas flow to carry the ions, we conclude that the ions would likely collide with one of the electrodes (depending on ion polarity) and become neutralized during their transfer through the deflector.

The ion travel time between the wire electrode and the steel tube is determined by the electric field, ion mobility, and electrode distances. To calculate the electric field, we assume a concentric cylindrical geometry between the inner wire electrode with r_1 radius (0.038 cm) and outer tube electrode with r_2 radius (0.24 cm). Potentials of V_1= +2500 V and V_2= +1500 V are applied to wire and tube electrodes, respectively.

The solution of the Laplace equation for cylindrical geometry yields the potential between the electrodes (V) as a function of radius (r):

$$V = C_1 \ln(r) + C_2 \quad (1)$$

where C_1 and C_2 are given by:

$$C_1 = (V_2 - V_1)/\ln(\frac{r_2}{r_1}) \quad (2)$$

$$C_2 = V_2 - C_1 \ln(r_2) \quad (3)$$

The electric field (E) between the electrodes is calculated from the derivative of potential with respect to r, yielding:

$$E(r) = C_1/r \quad (4)$$

The radial velocity of the ion at each radial distance (Vel) is given by:

$$Vel(r) = \mu E = \frac{dr}{dt} \quad (5)$$

where μ is ion mobility. Accordingly, the travel time of the ion between r_1 and r_2 as a result of the electric field between the electrodes can be calculated from the integral:

$$t = \int_{r1}^{r2} \frac{1}{\mu E} dr = \int_{r1}^{r2} \frac{r}{\mu C_1} dr = \frac{(r_2^2 - r_1^2)}{2\mu C_1} \quad (6)$$

Substituting values of V_1= +2500 V, V_2= +1500 V, r_1=0.038 cm, r_2 = 0.24 cm, and a typical mobility of μ=1 cm^2/Vs yields a travel time of 52 μs for ions to move from one electrode to the other.

Now we consider the travel time of species carried by the gas flow. The 100 mL/min of He gas flows through a quartz tube with a 0.05 cm radius, resulting in an average velocity of 2.1 m/s for species emerging from the quartz tube. A flow of 2.0 L/min of nitrogen is supplied to the post-plasma tee. This flow is introduced into the annular area between the quartz tube and the steel tube, resulting in average linear velocity of 3.0 m/s. The flow mixing dynamics is complex in this area. For simplicity and a conservative estimate, we use the higher velocity of 3.0 m/s. This velocity translates to 6.7 ms for the ions to pass through the 2-cm long deflection area composed of the concentric wire-tube geometry.

These estimates indicate that the ions collide with the electrodes in a time frame that is two-orders of magnitude shorter than the travel time through the deflector by the flow. Thus, we conclude that the ions

are efficiently eliminated by the deflector when the wire and the tube electrodes are biased to 2500 and 1500 V, respectively.

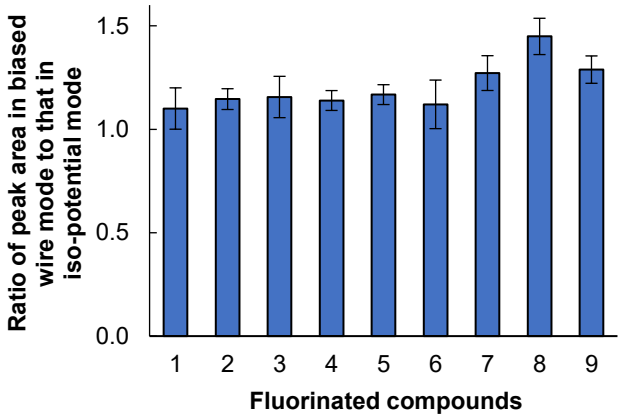

Figure S4. Effect of deflector operation mode on Na_2F^{-+} formation from various fluorochemicals in GC-DBD-nano-ESI -MS. The x axis indicates compounds in order of elution corresponding to those in Figure 2 (see Table S1 for compound names). The injected amount for each analyte is also identical to those of Figure 2. GC peak areas in biased wire mode (wire= 2500 V) are normalized to peak areas observed in iso-potential mode (wire= 1500 V) by monitoring Na_2F^+ in GC-DBD-nano-ESI-MS of Figure S3. Error bars reflect standard deviation of the measurements based on triplicate injections of the fluorochemical mixture in each mode. The Na_2F^+ formation in biased wire mode is not reduced compared to that in iso-potential wire-tube mode, suggesting that ionic species (e.g. F^-) from DBD do not contribute significantly to Na_2F^+ formation.

Post-plasma reactions of fluorine atom during transit time from plasma to nano-ESI

As noted above, the gas flow rates in the quartz plasma tube and within the steel post-plasma tube lead to average velocities of 2.1 m/s and 3.0 m/s. The neutral species travel 2 cm inside the quartz tube within the post-plasma tee. The species are then carried by the mix of nitrogen and helium for 3.5 cm within the steel tube. Therefore, a total travel time of 21 ms is estimated for neutral species within the tee assembly. The flow emerging from the post-plasma tube travels 0.5 cm prior to reaching the ESI tip. Assuming an upper bound 3 m/s velocity, this travel time would add 1.7 ms to the total travel time toward the ESI tip.

To evaluate the likelihood of F atom surviving this travel time, we consider reaction of F with water, a known impurity in gases. The presence of water is also confirmed by OH emissions from the plasma in Figure S2. A second-order reaction rate (k) of 1.46×10^{-11} cm^3/molecule·s is reported for the reaction:[3]

$$^{\bullet}F_{(g)} + H_2O_{(g)} \rightarrow {}^{\bullet}OH_{(g)} + HF_{(g)} \qquad (7)$$

Residual water is found in UHP gases at concentrations less than 2 ppmv. A 1 ppmv water impurity at atmospheric pressure and room temperature translates to 41 pmol/mL in gas phase. We note that the helium gas flow is heated within the pre-plasma tee. However, the gas quickly cools down as it travels through the quartz tube. A thermocouple inserted into the quartz tube registered temperature of 34 °C. Further, a much larger flow of nitrogen (2 L/min) is introduced into the post-plasma tee at room temperature. Thus, our estimates are not compromised by heating of helium in the pre-plasma tee.

To estimate the concentration of F atoms, we use the highest amount of F (1000 pg) we injected onto the column in the form of fluorinated compounds. Using an average full width at half maximum (FWHM) of 1 s for GC peaks, a helium flow rate of 100 mL/min, and the maximum possible (100%) conversion of F in organic molecules to F atom in the plasma, we estimate a maximum fluorine concentration of 31.6 pmol/mL in helium. Upon mixing with nitrogen, this value would further decrease while the concentration of water would stay the same because nitrogen also contains water. Therefore, there would be a minimum excess water of 9 pmol/mL. This excess water concentration translates to a half-life of 8.7 ms for F atoms based on pseudo-first order treatment of F-water reaction. For lower amounts of F, the half-life will reduce as there will be more water available throughout the reaction. Moreover, we

emphasize that this half-life is an upper bound estimate because dilution of helium in nitrogen keeps the water concentration higher than that calculated based on remaining water after reaction with all of F atoms. For comparison, assuming a constant 1 ppm water unaffected by F injection, a half-life of 1.9 ms is calculated. Higher water concentrations as impurity or caused by ambient air diffusion into the gas handling junctions would further reduce the half-life of F atoms. Accordingly, we infer that F atoms are unlikely to survive the transit to the ionization region, leaving HF as the likely neutral precursor for Na_2F^+ formation.

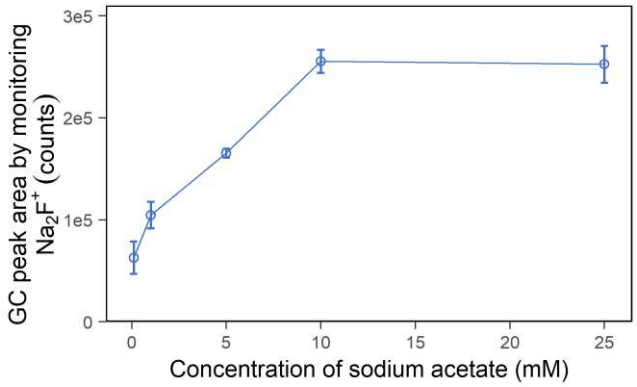

Figure S5. Effect of sodium acetate concentration (0.1, 1, 5, 10 and 25 mM) as nano-ESI electrolyte on the GC peak areas detected by monitoring Na_2F^+ upon injections of decafluorobiphenyl (499 pg F on-column) in GC-DBD-nano-ESI-MS. Error bars indicate standard deviations of GC peak areas from three experiments with a different nano-ESI tip used in each experiment.

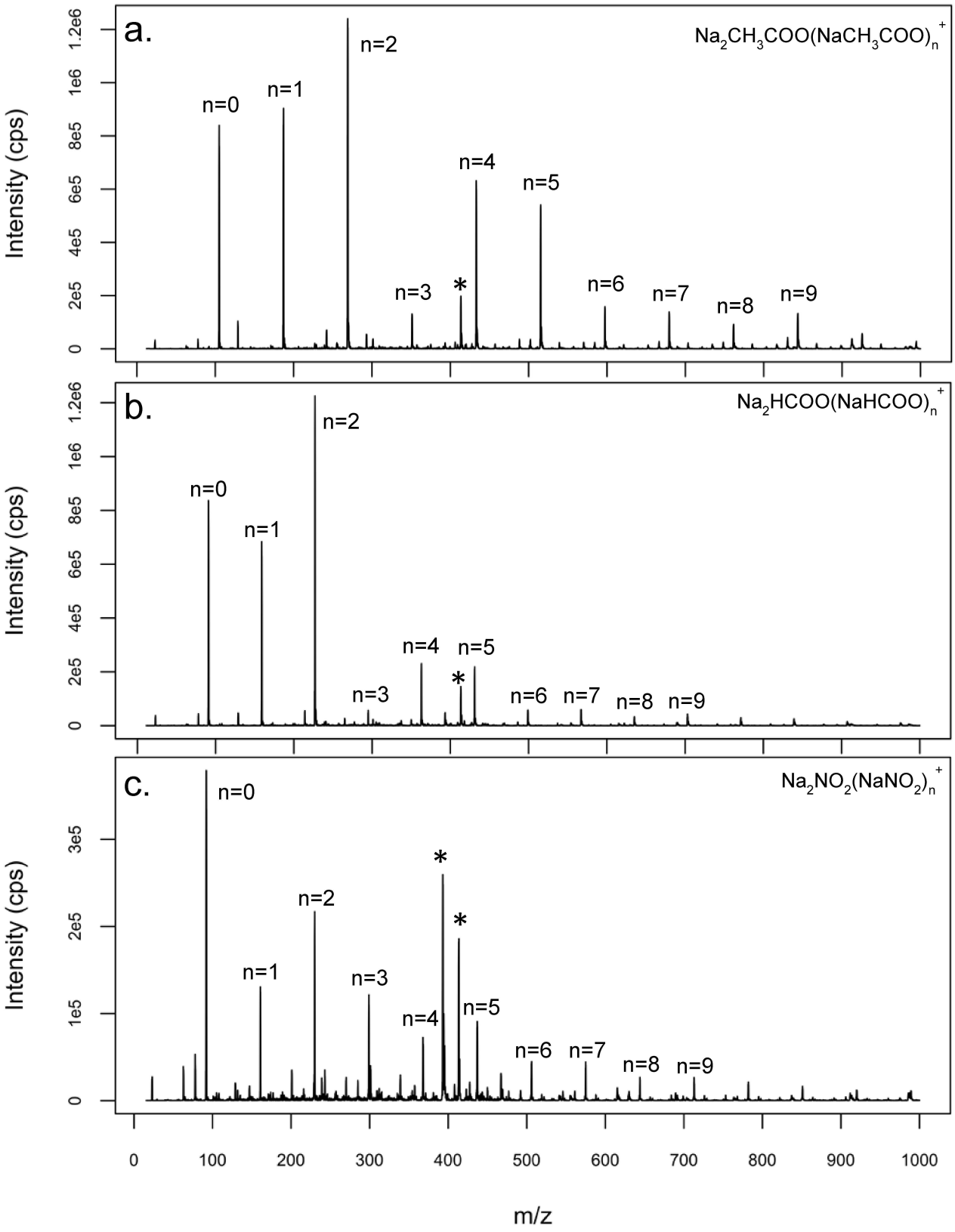
a.
$Na_2CH_3COO(NaCH_3COO)_n^+$
n=0
n=1
n=2
n=3
n=4
n=5
n=6
n=7
n=8
n=9
*
b.
$Na_2HCOO(NaHCOO)_n^+$
c.
$Na_2NO_2(NaNO_2)_n^+$
Intensity (cps)
0
2e5
4e5
6e5
8e5
1e6
1.2e6
1e5
2e5
3e5
0
100
200
300
400
500
600
700
800
900
1000
m/z

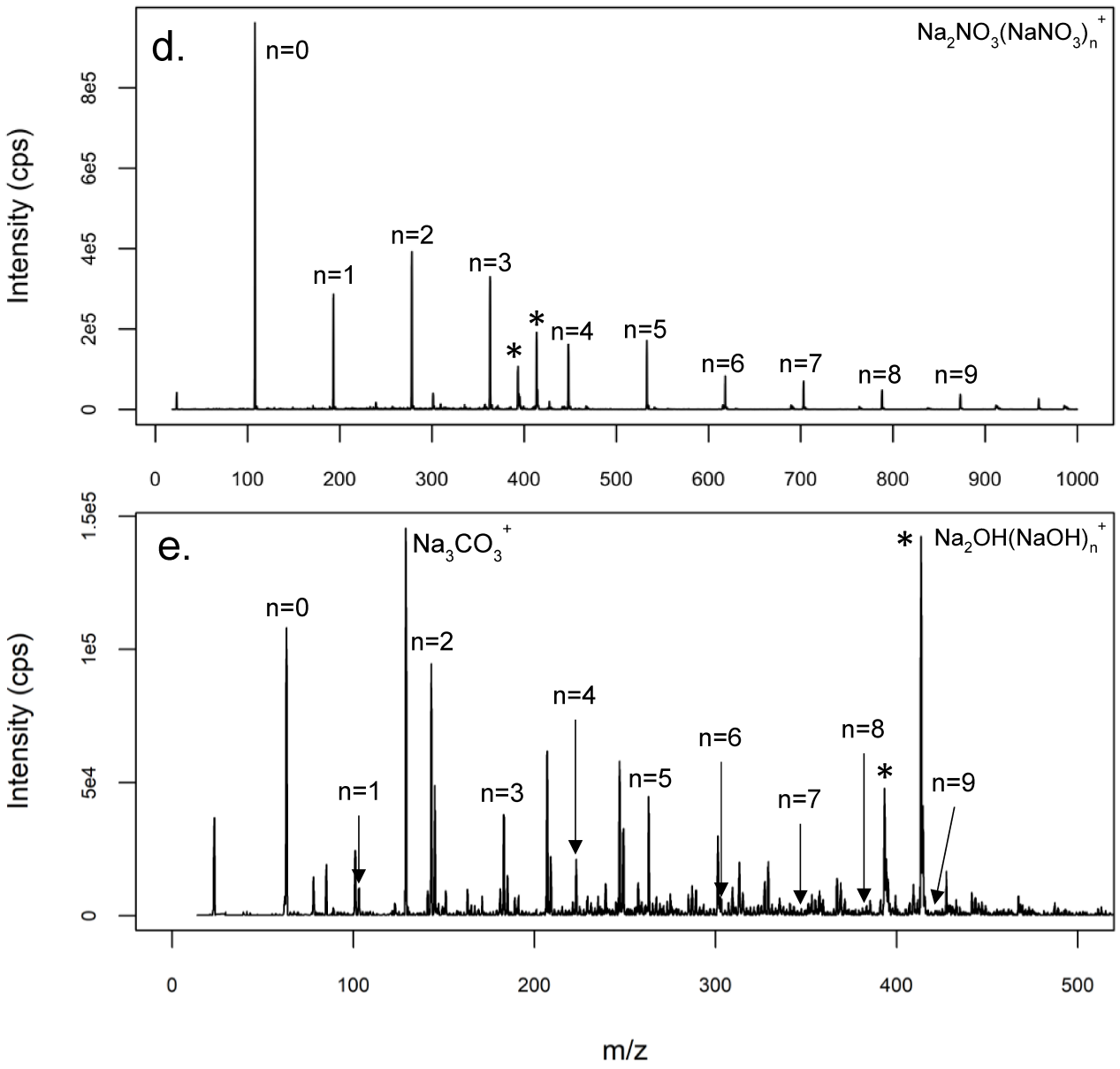

Figure S6. Background mass spectra using nano-ESI infusion of 10 mM electrolyte solutions: a) CH_3COONa, b) HCOONa, c) $NaNO_2$, d) $NaNO_3$, and e) NaOH. The asterisk (*) denotes the common contaminants observed in ESI spectra at m/z 393 ($[M+Na]^+$, dioctyl adipate) and 413 ($[M+Na]^+$, diisooctyl phthalate).

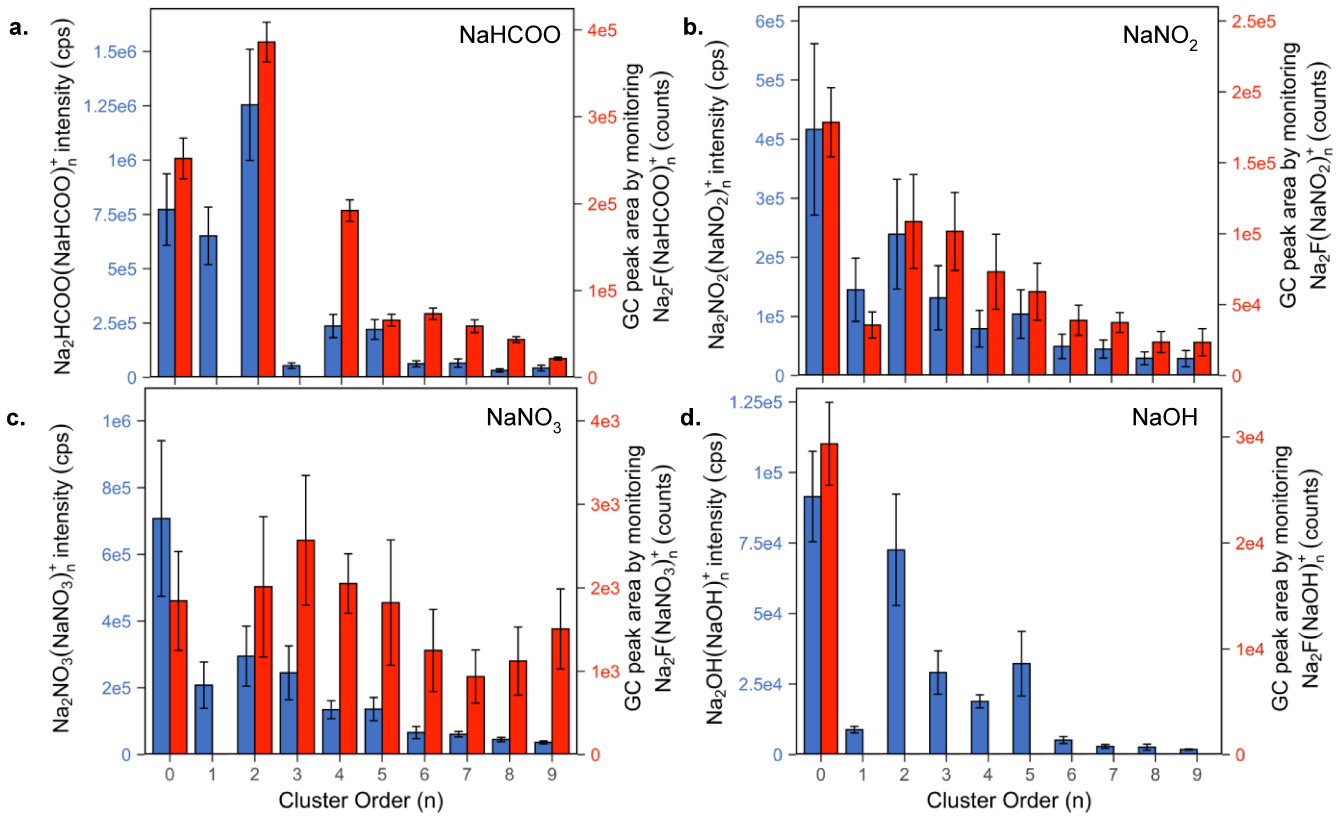

Figure S7. Cluster distributions of $Na_2A(NaA)_n^+$ (from nano-ESI) and $Na_2F(NaA)_n^+$ (from injections of 597 pg F on-column as decafluorobiphenyl in GC-DBD-nano-ESI-MS) using various 10 mM electrolytes: a) HCOONa, b) $NaNO_2$, c) $NaNO_3$, and d) NaOH. Error bars indicate standard deviations of ion intensities and GC peak areas from three experiments with a different nano-ESI tip used in each experiment. Different electrolytes produce varying cluster distributions for $Na_2A(NaA)_n^+$ and $Na_2F(NaA)_n^+$ ions.

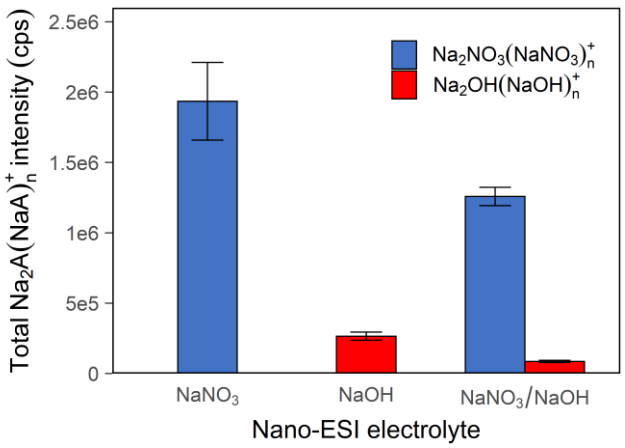

Figure S8. Total intensities of reagent ions $Na_2A(NaA)_n^+$ with n = 0-9 for NaNO3, NaOH and $NaNO_3$/NaOH electrolytes generated by nano-ESI infusion. Error bars reflect standard deviations of the total intensities from triplicate Q1 scans with each scan acquired using a new nano-ESI tip.

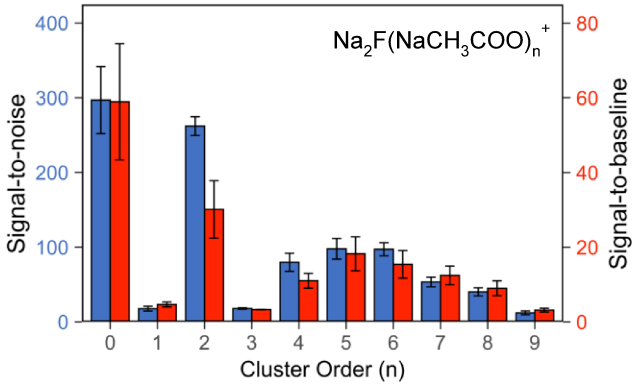

Figure S9. S/N (left axis, blue bars) and S/B (right axis, red bars) in GC-DBD-ESI-MS using cluster ions of $Na_2F(NaCH_3COO)_n^+$, with n = 0-9, as the analytical ion from injections of 597 pg F on-column as decafluorobiphenyl. Error bars indicate standard deviations from three experiments with a different nano-ESI tip used in each experiment. Na_2F^+ (n=0) has the highest S/B and S/N among all the clusters, and therefore is selected to characterize the analytical performance.

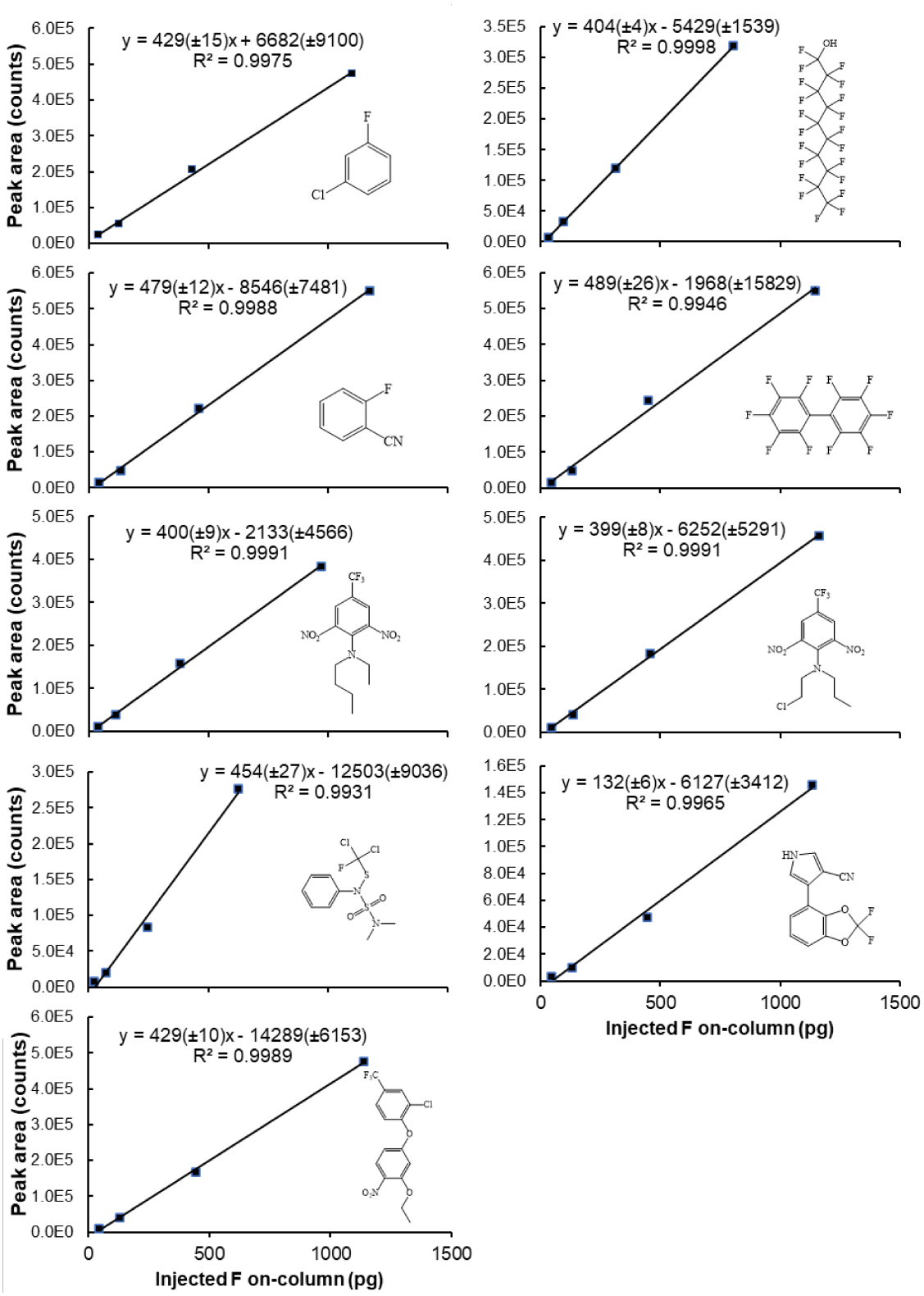

Figure S10. Peak areas in GC-DBD-nano-ESI-MS by monitoring Na_2F^+ as a function of injected fluorine amount (pg on-column) for different compounds. Standard errors of the regression parameters are shown in the parentheses.

Table S2. Limits of detection (LOD) in GC-DBD-nano-ESI-MS using Na_2F^+ as analytical ion

Elution order	Retention time (min)	Compound name	Formula and MW	Structure	LOD (pg compound on-column)	LOD (pg F on-column)
1	2.75	1-chloro-3-fluorobenzene	C_6H_4FCl MW=130.55	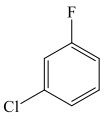	33	4.8
2	3.79	1H,1H,2H,2H-perfluoro-1-decanol	$C_{10}H_5F_{17}O$ MW=464.12	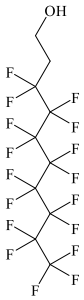	7.1	5.0
3	4.40	2-fluoro-benzonitrile	C_7H_4FN MW=121.12	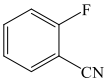	27	4.2
4	5.18	Decafluoro biphenyl	$C_{12}F_{10}$ MW=334.12	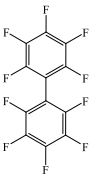	6.2	3.5
5	7.77	Benfluralin	$C_{13}H_{16}F_3N_3O_4$ MW=335.28	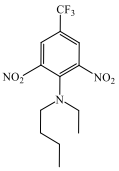	29	4.9
6	8.30	Fluchloralin	$C_{12}H_{13}ClF_3N_3O_4$ MW=355.7	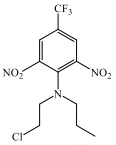	33	5.2
7	9.15	Dichlofluanid	$C_9H_{11}Cl_2FN_2O_2S_2$ MW=333.23	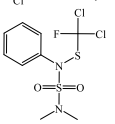	89	5.0
8	10.49	Fludioxonil	$C_{12}H_6F_2N_2O_2$ MW=248.19	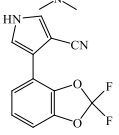	126	19
9	10.61	Oxyfluorfen	$C_{15}H_{11}ClF_3NO_4$ MW=361.7	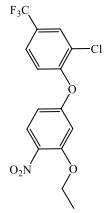	48	7.6

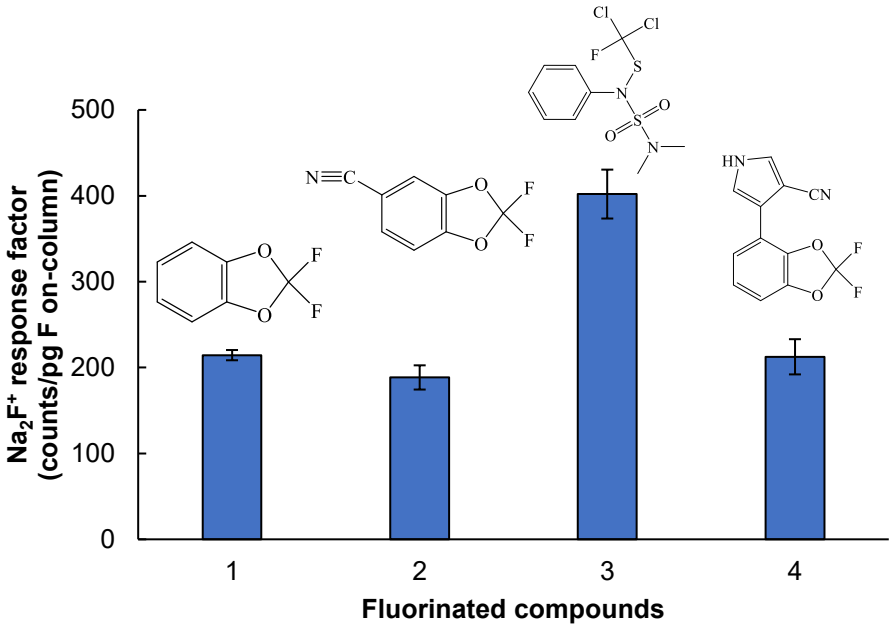

Figure S11. Response factors for analogs of fludioxonil (compound 4 above), sharing the 2,2-difluoro-1,3-benzodioxole motif, compared to that of fluchloralin (compound 3 above). Error bars reflect standard deviations from triplicate injections. The on-column injected amounts for compounds 1-4 above are: 2,2-difluoro-1,3-benzodioxole, 594 pg F; 2,2-Difluoro-1,3-benzodioxole-5-carbonitrile, 590 pg F; fluchloralin, 574 pg F; and fludioxonil, 622 pg F. Analytes with the 2-difluoro-1,3-benzodioxole motif show similar response factors but lower than that of fluchloralin, indicating incomplete breakdown of this motif in DBD.

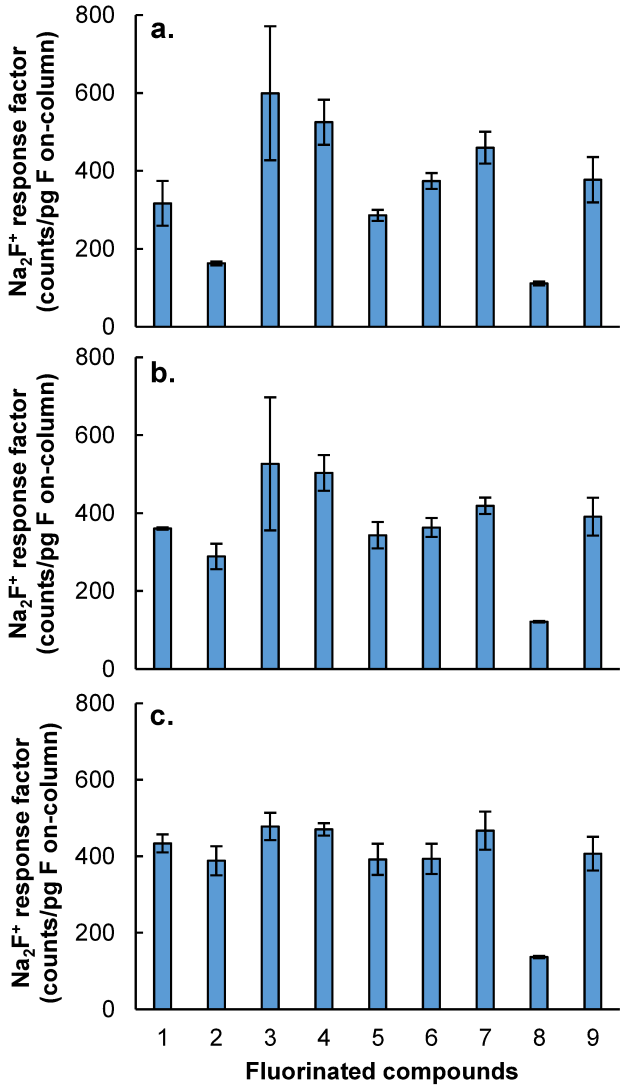

Figure S12. Effect of DBD operating parameters on response factors (RF) of 9 fluorinated compounds: a) 2.2 kV at 22 kHz, b) 4.1 kV at 22 kHz and c) 2.2 kV at 65 kHz. Error bars are standard deviations from triplicate injections. Numbers in x-axis indicate compounds in the order of elution in Figure 2 (see Table S2 for compound names and structures). The on-column injected amounts are the same as those in Figure 2. DBD operation at 2.2 kV at 65 kHz shows the best plasma reaction efficiency based on the near-uniform RF for 8 out of 9 compounds.

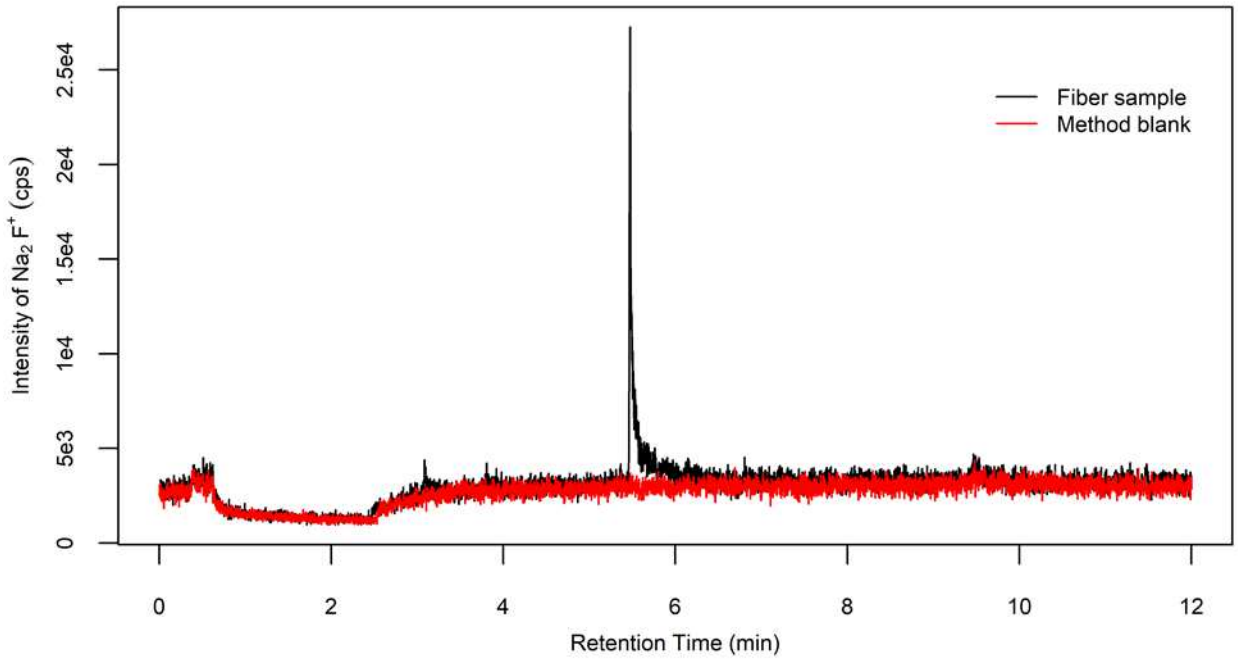

Figure S13. Overlay of Na_2F^+ chromatograms for extraction method blank (red trace) and Chico's fiber thread extraction using ethyl acetate (black trace).

References

1. Frisch, M. J.; Trucks, G. W.; Schlegel, H. B.; Scuseria, G. E.; Robb, M. A.; Cheeseman, J. R.; Scalmani, G.; Barone, V.; Petersson, G. A.; Nakatsuji, H.; Li, X.; Caricato, M.; Marenich, A. V.; Bloino, J.; Janesko, B. G.; Gomperts, R.; Mennucci, B.; Hratchian, H. P.; Ortiz, J. V.; Izmaylov, A. F.; Sonnenberg, J. L.; Williams; Ding, F.; Lipparini, F.; Egidi, F.; Goings, J.; Peng, B.; Petrone, A.; Henderson, T.; Ranasinghe, D.; Zakrzewski, V. G.; Gao, J.; Rega, N.; Zheng, G.; Liang, W.; Hada, M.; Ehara, M.; Toyota, K.; Fukuda, R.; Hasegawa, J.; Ishida, M.; Nakajima, T.; Honda, Y.; Kitao, O.; Nakai, H.; Vreven, T.; Throssell, K.; Montgomery Jr., J. A.; Peralta, J. E.; Ogliaro, F.; Bearpark, M. J.; Heyd, J. J.; Brothers, E. N.; Kudin, K. N.; Staroverov, V. N.; Keith, T. A.; Kobayashi, R.; Normand, J.; Raghavachari, K.; Rendell, A. P.; Burant, J. C.; Iyengar, S. S.; Tomasi, J.; Cossi, M.; Millam, J. M.; Klene, M.; Adamo, C.; Cammi, R.; Ochterski, J. W.; Martin, R. L.; Morokuma, K.; Farkas, O.; Foresman, J. B.; Fox, D. J. *Gaussian 16 Rev. C.01*, Wallingford, CT, **2016**.

2. Michels, A.; Tombrink, S.; Vautz, W.; Miclea, M.; Franzke, J., Spectroscopic characterization of a microplasma used as ionization source for ion mobility spectrometry. *Spectrochim. Acta Part B* **2007,** *62* (11), 1208-1215.

3. Stevens, P. S.; Brune, W. H.; Anderson, J. G., Kinetic and mechanistic investigations of fluorine atom+ water/water-d2 and fluorine atom+ hydrogen/deuterium over the temperature range 240-373 K. *J. Phys. Chem.* **1989,** *93* (10), 4068-4079.